

# Ice Nucleation Kinetics of Aerosols Containing Aqueous and Solid Ammonium Sulfate Particles

Hui-Ming Hung, Adam Malinowski, and Scot T. Martin\*

Division of Engineering and Applied Sciences, 29 Oxford Street, Pierce Hall, Room 122,  
Harvard University, Cambridge, Massachusetts 02138

Received: May 31, 2001; In Final Form: September 20, 2001

Ice freezing events in aerosols composed of  $(\text{NH}_4)_2\text{SO}_4/\text{H}_2\text{O}$  particles are studied for  $0 < x < 0.12$ , where  $x$  is the salt mole fraction composition. A segmented flow tube is employed to cool the aerosol and to adjust the aqueous particle composition in the first section, to freeze the aerosol in the second section, and to observe particle phase and composition with infrared (IR) spectroscopy in the third section. For the described experiments, three separate test aerosols are generated. The first test aerosol is composed of aqueous particles, while the other two aerosols contain a mix of aqueous and crystalline species. The IR spectra of these three different aerosols are similar, and the same apparent mole fraction composition is indicated for each based upon the ratio of band intensities. Although they have similar apparent mole fraction compositions, the observed ice freezing characteristics of the aerosols differ markedly from one another. The first aerosol, which consists entirely of aqueous particles, shows the deepest apparent supercooling. The freezing data, consisting of ice mass fraction versus temperature, are inverted by a model simulation to obtain homogeneous nucleation rates ( $J$ ) as a function of temperature ( $T$ ) and composition ( $x$ ).  $J(T, x)$  is provided for  $0 < x < 0.12$  and  $5 < \text{Log}_{10}J < 10$ , which is the range of  $J$  that can be probed with the current apparatus. At lower  $J$  values, which are associated with warmer temperatures, one particle in  $10^6$  nucleates ice homogeneously: the observed ice freezing event is then due to vapor-phase mass transport from the numerous surrounding supercooled aqueous particles to the few ice particles. In contrast, at higher  $J$  values, which are associated with cooler temperatures, one particle in 10 freezes by homogeneous nucleation.

## 1. Introduction

Understanding and quantifying the mechanisms of cirrus cloud formation are important steps in reducing uncertainty in models of global climate change.<sup>1–4</sup> One important pathway in cirrus cloud formation initiates with ice nucleation inside supercooled aqueous droplets.<sup>5–9</sup> Common aqueous chemical species in the upper troposphere include sulfuric and nitric acids, which have recently been found to be partially or wholly neutralized by ammonia in many cases. For these reasons, quantification of the rates of homogeneous ice nucleation in aqueous ammonium sulfate has recently been a major effort among laboratory groups.

The literature during the past two years shows that the freezing results obtained for  $(\text{NH}_4)_2\text{SO}_4/\text{H}_2\text{O}$  appear to disagree broadly. Several different techniques have been employed, including optical microscopy (OM),<sup>10</sup> differential scanning calorimetry (DSC),<sup>10</sup> continuous flow thermal diffusion chamber (CFD),<sup>11</sup> and several different aerosol flow tube studies employing infrared spectroscopy for ice detection (AFT-IR).<sup>12–14</sup> Even for a single technique, such as AFT-IR, there is large disagreement.<sup>12–14</sup> Cziczo and Abbatt<sup>13</sup> and Chelf and Martin<sup>14</sup> report freezing temperatures much warmer than Prenni et al.<sup>12</sup> Hung and Martin<sup>15</sup> provide a model simulation of ice freezing events for each technique to test the hypothesis that a single homogeneous nucleation rate function ( $J$ ) might be consistent with the different apparent freezing temperatures. One clear result is that the three AFT-IR results<sup>12–14</sup> cannot be reconciled.

In the current work, a third generation aerosol flow tube apparatus is constructed and experiments are conducted. Importantly, apparent agreement is obtained with the three previous AFT-IR studies of ice formation in  $(\text{NH}_4)_2\text{SO}_4/\text{H}_2\text{O}$  aerosols.<sup>12–14</sup> The key variable, new to the current study, is the mixing state of the aerosol. Three different kinds of aerosols are prepared, including one aerosol composed of aqueous particles, a second prepared by mixing crystalline particles with water vapor, and a third obtained by mixing separate streams of aqueous and crystalline particles. The IR spectra of these aerosols can appear similar (i.e., apparently of same chemical composition) while the ice freezing characteristics differ strongly.

## 2. Experimental Approach

The phase transitions of  $(\text{NH}_4)_2\text{SO}_4/\text{H}_2\text{O}$  particles are studied by employing a segmented AFT (Figure 1), in which the temperature and the aqueous particle composition are conditioned by heat and vapor exchange with the AFT walls and in which the freezing event is monitored by IR spectroscopy. The aerosol flow tube is segmented into a conditioning cell, a freezing cell, and an observation cell. IR spectroscopy is employed to determine the apparent aqueous mole fraction composition ( $x^*$ ) of the aerosol, as controlled by an aerosol conditioning temperature ( $T_c$ ). Candidate freezing temperatures ( $T_f$ ) are stepwise reduced until the freezing event is apparent,<sup>15</sup> which is designated as the apparent freezing temperature ( $T_f^*$ ). This vocabulary and the associated ideas are developed in detail by Hung and Martin.<sup>15</sup>

**2.1. Aerosol Generation.** The primary aerosol, composed of aqueous  $(\text{NH}_4)_2\text{SO}_4$  particles, is produced via a TSI 3076

\* Corresponding author. E-mail: scot\_martin@harvard.edu. Web: <http://www.deas.harvard.edu/~smartin>

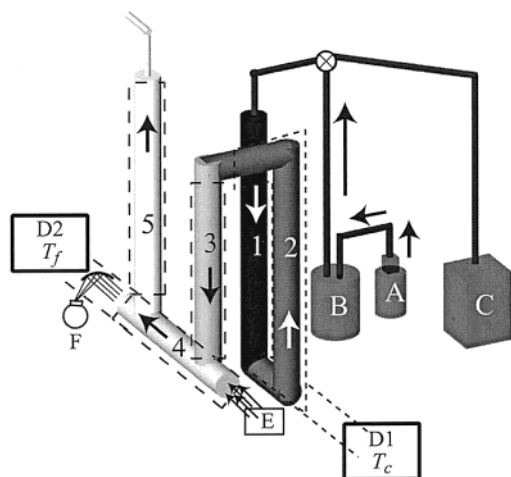


**Figure 1.** Schematic diagram of the experimental apparatus. Key: A, atomizer; B, preconditioning chamber; C, scanning mobility particle sizer (SMPS); D1 and D2, low-temperature circulators; E, modulated IR source; F, MCT-A IR detector; 1, preconditioning cell ( $T = 298$  K); 2, conditioning cell ( $T = T_c$ ); 3, freezing cell ( $T = T_f$ ); 4, observation cell ( $T = T_i$ ); and 5, exit cell ( $T = T_i$ ).

atomizer (35 psi, 3 slpm  $N_2$  flow). A 1 M  $(NH_4)_2SO_4$  aqueous reservoir solution is prepared in deionized water (18.3 M $\Omega$  cm). The primary aqueous aerosol is employed to generate three types of derivative aerosols for detailed studies, including one aerosol containing only aqueous particles, a second prepared by mixing crystalline particles with water vapor ("mixed aerosol #1"), and a third obtaining by mixing separate streams of aqueous and crystalline particles ("mixed aerosol #2").

The first type of derivative aerosol is simply the primary aerosol itself. The particles are fully deliquesced, which is verified via a diagnostic indicator (q.v. section 2.4.2) in the IR spectrum of the sulfate peak ( $1100\text{ cm}^{-1}$ ) at 223 K. The second type of derivative aerosol (viz. mixed aerosol #1) is prepared by passing the flow of the primary aerosol through a drying chamber ( $RH < 7\%$ ) and then mixing, in a baffled chamber at 298 K, this flow of dry aerosol with a regulated flow of water vapor from a bubbler humidifier. For mixed aerosol #1, diagnostic indicators are present for both crystalline ammonium sulfate (viz. a shoulder at  $1100\text{ cm}^{-1}$  on the sulfate peak below 223 K) and aqueous ammonium sulfate (viz. condensed-phase water at  $1650\text{ cm}^{-1}$ ).

The third type of derivative aerosol (viz. mixed aerosol #2) is prepared by dividing the primary aerosol flow in half to create two secondary flows. One secondary flow passes through a drying chamber ( $RH < 7\%$ ) while the other remains humid. The dry and humid secondary flows, respectively, referred to hereafter as secondary flows #1 and #2, are remixed at low temperatures in the flow tube apparatus. Secondary flow #2 enters the apparatus via the main inlet, i.e., flowing through the preconditioning, conditioning, freezing, observation, and exit cells. Secondary flow #1 enters the cold region directly, through an auxiliary port on the freezing cell; this aerosol flows through the freezing, observation, and exit cells. Therefore, the two aerosol flows are mixed together prior to entering the observation cell.

The number size distribution of the dry aerosol in the primary flow is characterized by a scanning mobility particle sizer (SMPS) (TSI 3934). The aerosol in the current study has a dry mode diameter of 300 nm and a number density of  $6 \times 10^6$  #-particles/ $\text{cm}^3$ -gas. These values differ somewhat from our earlier experimental work.<sup>14</sup> However, in that work no strong dependence is reported for the freezing characteristics of three

aerosols characterized by different number size distributions. The respective mode sizes and number concentrations of the three aerosols in the earlier work are 150 nm and  $2.34 \times 10^7$  #-particles/ $\text{cm}^3$ -gas, 300 nm and  $1.92 \times 10^7$  #-particles/ $\text{cm}^3$ -gas, and 400 nm and  $4.31 \times 10^6$  #-particles/ $\text{cm}^3$ -gas. Hung and Martin<sup>15</sup> simulate the freezing properties of these aerosols and find little difference in the apparent freezing temperatures (i.e., within 2–3 K).

Some concern has been expressed that the atomization method for aerosol generation possibly yields the inclusion in the aqueous droplets of insoluble impurities, which could behave as heterogeneous nuclei toward  $(NH_4)_2SO_4$  crystallization. However, Chelf and Martin<sup>14</sup> find no difference between the ice freezing events of aerosols generated by atomization and aerosols generated by vapor condensation, which is an approach that excludes impurities. The main difference is that atomization of the  $(NH_4)_2SO_4$  solution produces an aerosol with a higher total water content, as compared to the drier aerosol produced via the vapor condensation approach.

**2.2. Aerosol Preconditioning.** Several setups are employed at 298 K to adjust the water content of the aerosol, after its generation but prior to its entering the low-temperature flow tubes of the apparatus. Depending on the type of experiment, different aerosol characteristics are desired and can be obtained with one of 0.1, 1, 2, 4, or 8 M  $H_2SO_4$  solutions (ca. 500 mL) in a 6-L Erlenmeyer flask (i.e., the preconditioning chamber). Aerosol entering the preconditioning chamber exchanges water vapor with the solution (though without achieving equilibrium during the short 2 min residence time), thus adjusting the aerosol water vapor pressure and, in consequence, the condensed-phase aqueous composition. To produce a dry aerosol containing crystalline particles ( $RH < 11\%$ ), solutions of either concentrated  $H_2SO_4$  or saturated LiCl solution are employed.

**2.3. Low-Temperature Flow Tubes.** The experiments are conducted with a new AFT apparatus, based upon experience gained in our earlier work.<sup>14</sup> The apparatus, suspended from the ceiling, consists of seven sections of 2 in. i.d. straight copper tubes joined by 2 in. i.d. "U-shaped" sections (Figure 1). The combined set of tubes is described succinctly by three functional regions, including conditioning, freezing, and observation cells. The aerosol flows from the preconditioner (section 2.2) through 1/2 in. i.d. polyethylene tubing and enters the low-temperature (LT) apparatus, where the diameter is increased to 2 in. The inlet of the LT apparatus is a single 100-cm long tubing section with no coolant flow in the outer coil (298 K). This section is a flow straightener. Passing through the first U-section, the aerosol enters the conditioning cell, where the temperature is controlled by the first circulating bath. The conditioning cell consists of three 2 in. i.d. tubing sections, totaling 153 cm in length. The temperature along the conditioning cell decreases steadily from 298 K at the junction with the flow straightener until reaching the conditioning temperature ( $T_c$ ) at the junction with the freezing cell.

Exiting the conditioning cell, the aerosol flows into the freezing cell (31 s residence time at 3 slpm flow), which is 76 cm long. The temperature drops over 30 cm to a candidate freezing temperature ( $T_f$ ), which is typically between 208 and 233 K. When ice forms in the aerosol, it is detected downstream in the next AFT section, which is the IR observation cell. The observation cell (23 s residence time at 3 slpm flow) is 56 cm long and capped at the ends with AgCl windows. A collimated IR beam (Nicolet Nexus 670 FTIR), which is modulated by a Michelson interferometer, passes along the axis of the observation cell and is collected with an off-axis parabolic mirror and

focused onto the active area of a mercury cadmium telluride (MCT-A) detector.

The aerosol passing through the observation cell next enters the exit cell, which is a 100 cm long tube and which exhausts the low-temperature flow tubes into laboratory hood lines through 1/2 in. diameter polyethylene tubing. The temperature in the exit cell is not crucial; however, the exit cell is chilled to minimize temperature gradients in the observation cell, which is in direct contact with the exit cell. The exit cell also preserves the laminar flow through the observation cell by avoiding upstream turbulence that would be associated with a more abrupt exit. The junctions from the freezing tube to the observation tube and from the observation tube to the exit tube are smoothly curved from a cut section of "U" tube. Although we do not directly sample the flow field through these junctions, literature supports that laminar flow should be maintained at the flow rates employed in the experiments.<sup>16</sup>

The flow tubes are cooled via copper tubing (1/4 in. o.d.) wrapped and soldered onto the outside of the flow tubes. Coolant (Syltherm) flow passes from two low-temperature circulating baths (Neslab ULT-80). As shown in Figure 1, connections are made to provide a conditioning temperature ( $T_c$ ) controlled by one circulator and a freezing/observation temperature ( $T_f$ ) controlled by the second circulator. The flow tubes are insulated with two layers of elastomer foam (1 in. thick) to slow the heat transfer between the cell and the laboratory surroundings. The coolant flow is split between the freezing and observation cells, so they are isothermal (excluding the transition region from the conditioning cell into the freezing cell), as verified by in situ thermistor probes.

The new apparatus offers at least four distinct advantages. First, the constant 2 in. diameter throughout all cold regions supports laminar flow in the system while avoiding problems of ice build-up and plugging previously encountered with flow tubes joined by smaller diameter sections. Second, the high thermal transfer coefficient of copper, as compared to glass, reduces temperature gradients while also making possible accurate external temperature measurements. The overall effect is lower ultimate temperatures. Third, freezing and observation are decoupled: the aerosol freezes in one tube and its IR spectrum is observed in the next. Fourth, the windows are housed in custom-made plastic cards that allow their easy insertion and removal for cleaning (5 min procedure), which is an important practical improvement over earlier versions of our apparatus because ice and salt deposit onto the windows.

**2.4. Infrared Spectra.** Ten scans are typically collected at 4  $\text{cm}^{-1}$  resolution in the absorbance mode. The apparent absorbance is actually extinction, containing contributions both from absorbance and from scattering by the particles. During data processing, spectral features from  $\text{H}_2\text{O}(\text{g})$  are routinely subtracted. Spectra are usually presented with the  $\text{CO}_2(\text{g})$  window omitted. The IR spectra are employed for several purposes, including (a) the determination of the apparent aqueous composition of the condensed phase based upon the integrated intensity of the water band relative to the sulfate band, (b) the determination of the presence or absence of crystalline ammonium sulfate in the aerosol (i.e., diagnostic indicator), and (c) the determination of apparent ice freezing temperatures.

**2.4.1. Determination of Apparent Aqueous Particle Concentration.** The apparent aqueous mole fraction composition ( $x^*$ ) of the  $(\text{NH}_4)_2\text{SO}_4/\text{H}_2\text{O}$  aerosol is determined from the IR spectrum based on a calibration curve<sup>14</sup> relating the dependence of aqueous composition on the peak area ratio of the 1751–

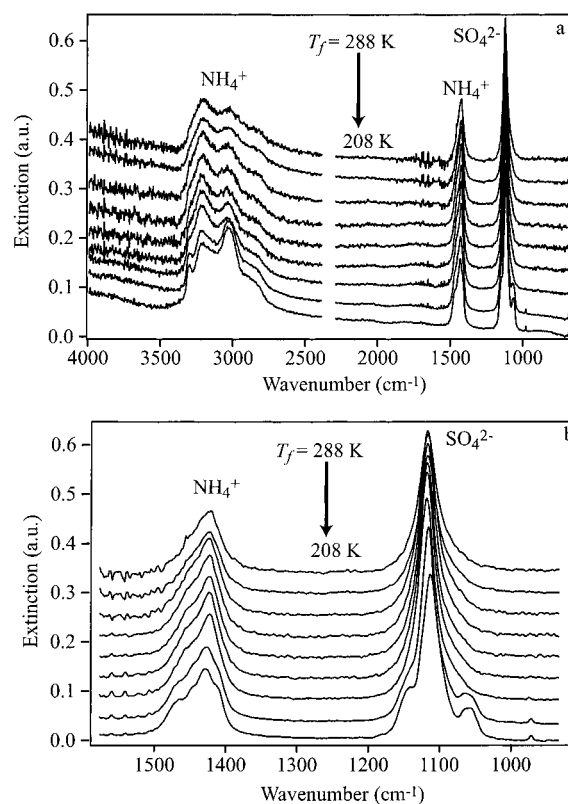


**Figure 2.** Spectral changes with cooling of an aerosol containing  $(\text{NH}_4)_2\text{SO}_4(\text{s})$  particles. (a) IR spectra of flowing crystalline  $(\text{NH}_4)_2\text{SO}_4$  aerosol as the freezing and observation cells are jointly cooled from  $T_f = 288$  to 208 K. (b) Expanded data for ammonium ( $1450 \text{ cm}^{-1}$ ) and sulfate ( $1100 \text{ cm}^{-1}$ ) regions. Conditions:  $T_c = 256 \text{ K}$  for  $T_f < 256 \text{ K}$  and  $T_c = T_f$  for  $T_f > 256 \text{ K}$ , 3 slpm,  $0.3 \text{ g-particles/m}^3 \text{ gas}$ ,  $6 \times 10^6 \text{ #-particles/cm}^3 \text{ gas}$ . Spectra are offset for clarity.

1549  $\text{cm}^{-1}$  water band to the 1180–1025  $\text{cm}^{-1}$  sulfate band for aqueous  $(\text{NH}_4)_2\text{SO}_4$ . The calibration curve follows from the optical constants of  $(\text{NH}_4)_2\text{SO}_4$  solutions measured by attenuated total reflectance IR spectroscopy.<sup>14</sup> An advantage of this technique is the minimal error ( $<0.1 \text{ wt } \%$ ) associated with the aqueous mole fraction ( $x$ ) of the solutions. A disadvantage is that calibration beyond salt saturation is possible only by extrapolation. The calibration curve is (the ratio of the water-peak-area to the sulfate-peak-area) =  $0.112 + 1.49 e^{-34.9x} + 7.07 e^{-181x}$ , where  $x$  is the mole fraction of aqueous  $(\text{NH}_4)_2\text{SO}_4$ . The uncertainty in the composition determination increases with higher  $(\text{NH}_4)_2\text{SO}_4$  mole fractions due to increasing uncertainties both in the calibration curve and in the peak area ratio determination, which arise from the small integrated absorption of condensed-phase water at higher  $(\text{NH}_4)_2\text{SO}_4$  mole fractions.

**2.4.2. Diagnostic Indicator.** Temperature-dependent spectra of  $(\text{NH}_4)_2\text{SO}_4(\text{s})$  aerosol are shown in Figure 2a from 288 to 208 K. As expected, large changes are apparent at  $T_f \leq 223 \text{ K}$  where the ferroelectric phase forms. Prior to this phase transition, the 1100  $\text{cm}^{-1}$  sulfate peak becomes sharper and more intense with cooling (Figure 2b), as expected from the decrease in crystal phonon energy, which broadens the peak at warmer temperatures. The 1100  $\text{cm}^{-1}$  peak is symmetric because sulfate in the paraelectric structure has tetrahedral symmetry.<sup>17,18</sup> The 1420  $\text{cm}^{-1}$  ammonium peak, including a high wavenumber shoulder, similarly sharpens at colder temperatures. The ferroelectric transition at  $T_f \leq 223 \text{ K}$  is accompanied by the appearance of several shoulders on both the ammonium and sulfate peaks.



As compared to  $(\text{NH}_4)_2\text{SO}_4(\text{aq})$ , the  $1420\text{ cm}^{-1}$  ammonium band of paraelectric  $(\text{NH}_4)_2\text{SO}_4(\text{s})$  is both red-shifted by  $30\text{ cm}^{-1}$  and asymmetric (i.e., the shoulder is absent in the aqueous spectrum). This asymmetric characteristic of the crystalline phase is a key spectral feature for distinguishing among aerosol types (i.e., entirely aqueous aerosol versus mixed aqueous/crystalline aerosols described in section 2.1).

**2.4.3. Determination of Apparent Freezing Temperatures.** Prior to freezing, as  $T_f$  falls, no significant IR spectral changes are observed. Thus, when two spectra at different temperatures are subtracted, the result is a flat line. (At sufficiently small tolerance, small spectral changes can appear due to the dependence of optical constants on the temperature.) In contrast, once ice forms, there are large changes in the difference spectra. To provide objective assignments of freezing temperatures, we calculate the temperature-normalized variance of the difference spectra and plot that variance versus  $T_f$ .<sup>14</sup> The apparent freezing temperature ( $T_f^*$ ) is defined as the local maximum. As a test of this analysis method,  $T_f^*$  values agree for three different spectral ranges, including  $690\text{--}880$ ,  $3290\text{--}3580$ , and  $650\text{--}4000\text{ cm}^{-1}$ . Even so, the variance calculation at  $(3290\text{--}3590\text{ cm}^{-1})$  region is strongly influenced by the coupling of scattering, hygroscopicity, and ammonium absorption. We find the  $690\text{--}880\text{ cm}^{-1}$  region is the most useful for delineating ice freezing events.

**2.5. Temperature Characterization.** Temperatures in the various regions of the low-temperature copper flow tubes are measured by 10 thermistors, which are joined to the tubes with thermoconductive tape.  $T_f$  is measured with a thermistor placed at the coldest point in the freezing cell. Agreement between externally measured temperatures with temperatures inside the AFT is verified periodically by inserting an additional thermistor into the freezing and observation cells. Several readings are taken at different depths along the cells and at different temperature conditions. The agreement between the two different sensors and among all tested positions in the freezing and observation cells (i.e., total temperature gradients) is within 1 K.

The ferroelectric phase transition at 223 K of  $(\text{NH}_4)_2\text{SO}_4$  provides a valuable diagnostic to assess temperature accuracy and gradients. For these measurements,  $T_c$  is fixed at 220 K to generate ferroelectric  $(\text{NH}_4)_2\text{SO}_4$ .  $T_f$  is then increased stepwise from 217 K. The phase transition would be observed as a delta function at 223 K in a perfectly isothermal apparatus (excluding any kinetic effects in the phase transition and any particle size effects on the thermodynamics). The IR spectra in Figure 3a show actual observations of the transition in the apparatus. As  $T_f$  warms past 223 K, the shoulders characteristic of the ferroelectric phase disappear (Figure 3a). To analyze the spectra for the possible appearance of a delta function, we take the difference spectra at consecutive temperatures, as plotted in Figure 3b. Large changes are apparent for the temperature increase from 222.7 to 223.2 K. The temperature-normalized variance of the difference spectra in the  $1050\text{--}1170\text{ cm}^{-1}$  region (viz. the sulfate peak) highlights the spectral changes. The variance as a function of  $T_f$  is shown in Figure 3c. As expected, the maximum variance occurs at 223 K,<sup>17</sup> which confirms the absolute accuracy of the temperature measurements, while the half-height bandwidth is under 1 K. Because the ferro- to paraelectric transition is sharp (i.e., similar to ice melting at 273 K), any apparent temperature dispersion in the transition (see Figure 3c), as compared to an idealized delta function, reveals temperature gradients in the apparatus. The temperature gradient of 1 K indicated by the half-height bandwidth agrees

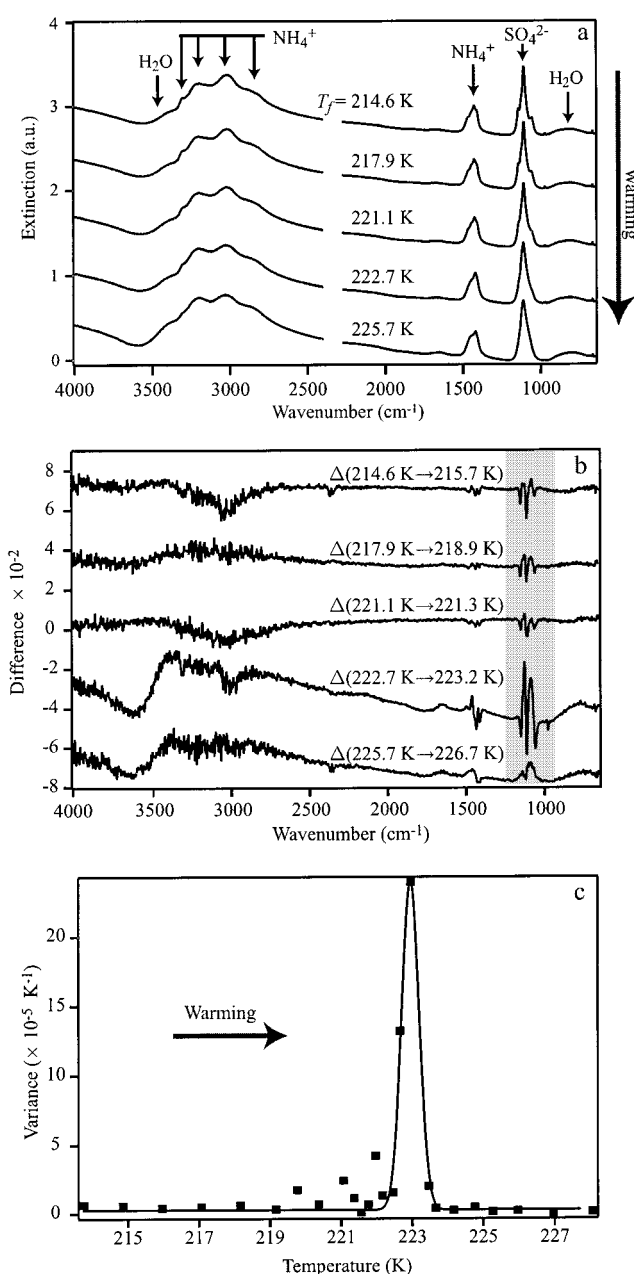


**Figure 3.** Apparatus temperature gradients are investigated by the ferroelectric phase transition of  $(\text{NH}_4)_2\text{SO}_4$ . Some condensed-phase water is also present in the aerosol, as seen in the spectra.  $T_c = 220\text{ K}$ . (a) IR spectra recorded as the freezing and observation cells are jointly warmed from  $T_f = 215$  to  $226\text{ K}$ . Spectra are offset for clarity. (b) Difference spectra obtained after subtraction of consecutive IR spectra. Gray bar marks the sulfate region ( $1050\text{--}1070\text{ cm}^{-1}$ ). (c) Temperature-normalized variance of the difference spectra in the  $1050\text{--}1070\text{ cm}^{-1}$  region. Solid lines serve to guide the eyes and do not represent a model fit. Conditions: 3 slpm,  $0.4\text{ g-particles/m}^3$  gas,  $8 \times 10^6$  #-particles/ $\text{cm}^3$  gas.

with that found by probing with inserted thermistors (under flow conditions). This gradient is a large improvement when compared to the 10 K temperature gradient in the previous version of our apparatus.<sup>14</sup> Measurements are also done in the reverse direction by setting  $T_c = 230\text{ K}$  and stepwise cooling  $T_f$  to observe the para- to ferroelectric transition. Similar results are obtained. There is no kinetic inhibition in the phase transition, which is generally believed to be first-order.<sup>19–21</sup> In short, Figure 3 confirms accurate temperature measurement and acceptable temperature gradients in the apparatus.

The recorded extinction spectra (Figure 3a) also have contributions (a) from light scattering by the particles, as shown in the sloping baseline toward higher wavenumbers, and (b) from condensed-phase water in the aerosol. The condensed-phase water arises in these spectra due to insufficient drying in the preconditioning chamber for the selected experiments. More thorough drying procedures, including a longer residence time, yield spectra without condensed-phase water, as shown in Figure 2.

**2.6. Procedure and Operation.** In a typical experiment,  $T_c$  and  $T_f$  are first set equal and adjusted together to regulate the apparent aqueous aerosol composition to approximately the desired  $x^*$  for a given experiment. For the range of  $x^*$  investigated,  $T_c$  lies between 250 and 271 K in all cases. Within the conditioning cell the aqueous aerosol exchanges vapor with ice on the walls, which is deposited earlier during an apparatus equilibration step at 215 K. Full equilibration, however, is not obtained during the transit time (60 s) through the conditioning cell. That is, the aqueous mole fraction composition of the aerosol is not in equilibrium with the vapor pressure over ice. The exact set point temperature for each investigated value of  $x^*$  is obtained by empirical feedback, in which we observe the IR spectrum and adjust  $T_c$  until an aerosol with approximately the desired apparent mole fraction composition is obtained (cf. section 2.4.1).

Once  $T_c$  is fixed, we then cool the freezing/observation cells further. At warm  $T_f$  values, the approximate  $x^*$  continues to change as  $T_f$  is cooled. At sufficiently low  $T_f$ , however,  $x^*$  no longer changes with further cooling (at least prior to ice formation) because the water vapor pressures are sufficiently low and the aerosol residence time is sufficiently short that vapor-phase mass transport from the walls does not affect aerosol condensed-phase water content. This fact is verified through control experiments in which  $T_f$  is dropped without affecting the aerosol IR spectrum, as explained by Chelf and Martin.<sup>14</sup> At sufficiently low  $T_f$ , we then determine the exact  $x^*$  for a given experiment. As a matter of course,  $x^*$  is typically determined in the range  $233 < T_f < 243$  K. These temperatures are warm enough that freezing does not occur, while they are cool enough that vapor exchange with the walls is not significant. The latter fact is verified by the absence of spectral changes prior to ice formation. These temperatures are also cold enough that gas-phase water lines contribute negligibly to the observed spectra, for which correction (and associated experimental error) would otherwise be necessary.

Once the composition is determined,  $T_f$  is cooled to 208 K and an IR spectrum (usually indicating ice) is recorded.  $T_f$  is subsequently warmed stepwise to 240 K while IR spectra are recorded. This approach of scanning temperature upward (as opposed to downward) is convenient because temperature equilibrium is obtained more rapidly. Smaller temperature gradients are also observed throughout the AFT. After the experiments, the spectra are analyzed off-line by plotting variance versus temperature (section 2.4.3).

### 3. Results

**3.1. Ice Freezing Event in an Aerosol Containing Aqueous Particles.** Figure 4 shows our approach to determining apparent freezing temperatures ( $T_f^*$ ). In Figure 4a, the IR spectra are shown for an aerosol containing aqueous particles of  $x^* = 0.070 \pm 0.008$  when cooled from 223 to 216 K. Spectral features of ice<sup>22</sup> (viz. a blue-shift and the appearance of a shoulder on the 3200  $\text{cm}^{-1}$  band and a blue-shift and intensity increase of the 650  $\text{cm}^{-1}$  band) are apparent at the lower end of the temperature

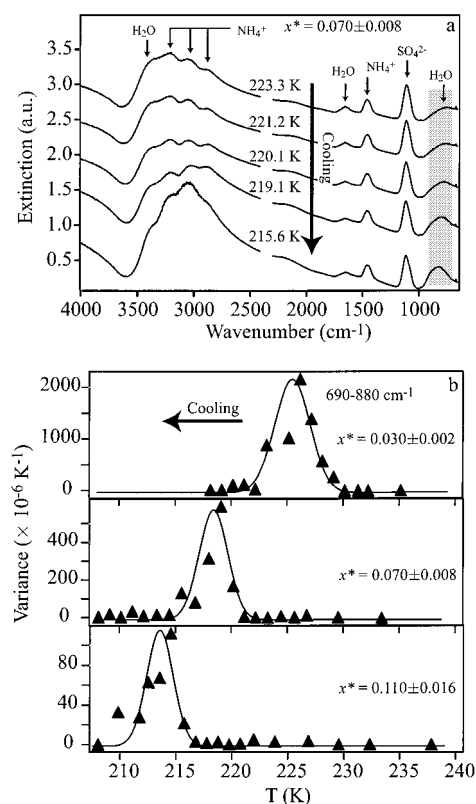


**Figure 4.** Detection of ice formation and assignment of apparent freezing temperature ( $T_f^*$ ). (a) IR spectra of flowing  $(\text{NH}_4)_2\text{SO}_4/\text{H}_2\text{O}$  aerosol as the freezing and observation cells are jointly cooled from  $T_f = 223$  to 216 K. Ice appears below 220 K. Spectra are offset for clarity. (b) Temperature-normalized variance of the difference spectra in the region of 690–880  $\text{cm}^{-1}$  (gray bar) for  $x^* = 0.03$ , 0.07, and 0.11. The respective apparent freezing temperatures are taken as the maxima in the variance plots. Solid lines serve to guide the eyes and do not represent a model fit. Conditions:  $T_c = 256$  K, 3 slpm, 0.3 g-particles/ $\text{m}^3$  gas,  $6 \times 10^6$  #-particles/ $\text{cm}^3$  gas. Ratio of the liquid water band (1650  $\text{cm}^{-1}$ ) to the sulfate band (1100  $\text{cm}^{-1}$ ) in aqueous particles yields the apparent aqueous mole fraction ( $x^*$ ).

range. Changes in light scattering also accompany the ice freezing event in this aerosol. To quantify the exact point of the phase transition, we take difference spectra and plot the temperature-normalized variance for the 690–880  $\text{cm}^{-1}$  range, as shown in Figure 4b. The apparent freezing temperature is taken at the maximum of the variance plot. To assist in further analysis, the data points are approximated by an empirical fit to a Gaussian curve. Similar variance plots are also shown in Figure 4b for  $x^* = 0.030 \pm 0.002$  and  $x^* = 0.110 \pm 0.016$ . It is seen that  $T_f^*$  falls steadily with increasing  $x^*$ .

Figure 4b shows that the absolute variance (i.e., the y-axis scale) in the region 690–880  $\text{cm}^{-1}$  decreases with increasing  $x^*$ . The probable explanation for variance (i.e., Figure 4b) is that the total aerosol water content in the aerosol decreases with increasing  $x^*$ ; the loading of  $(\text{NH}_4)_2\text{SO}_4$  in the aerosol is independent of  $x^*$ . Other contributions to the variance, especially above 1000  $\text{cm}^{-1}$ , are changes in light scattering, which accompany changes in aerosol number size distributions during the freezing event (i.e., growth of ice particles and shrinkage of aqueous particles), and changes in aqueous mole fraction composition (i.e., cryogenic pumping) that alter the infrared spectra.

In our earlier modeling work,<sup>15</sup> the ice freezing event is defined as 10% ice mass fraction freezing (i.e., the foot of Figure 4b) based upon experimental work that defined  $T_f^*$  as the onset

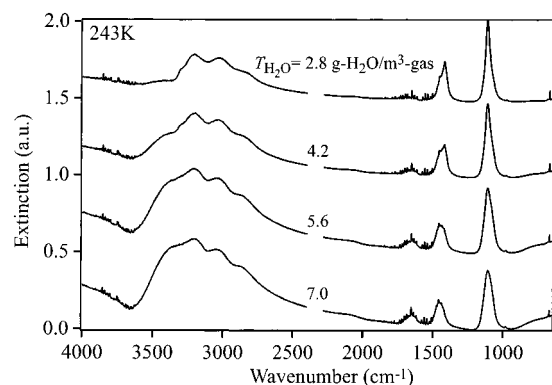


**Figure 5.** IR spectra of mixed aerosol #1 at  $T_f = 243$  K. To form this aerosol, flowing particles are equilibrated at 16, 24, 32, and 40% RH at 298 K, passed through the conditioning cell ( $T_c = 271$  K), and cooled to the observation temperature ( $T_f = 243$  K) where the shown IR spectra are recorded. Spectra are offset for clarity. Conditions: total water content ( $T_{H_2O}$ , g/m<sup>3</sup>) = 2.8, 4.2, 5.6, and 7.0 at 16, 24, 32, and 40% RH, respectively, 3 slpm aerosol flow, 0.3 g-particles/m<sup>3</sup> gas,  $6 \times 10^6$  #-particles/cm<sup>3</sup> gas. Spectra are offset for clarity

of observed ice formation. In the present experimental work,  $T_f^*$  is redefined as the maximum in the variance plot, which corresponds to approximately 50% ice mass fraction freezing. Correspondingly, this new definition is also adopted for the modeling work in this paper as the criterion of a positive ice freezing event. The change in definitions shifts  $T_f^*$  about 2 K cooler in most cases.

**3.2. Characterization of Mixed Phase Aerosols.** **3.2.1. Mixed Aerosol #1.** Figure 5 shows the IR spectra obtained by steadily increasing the total water vapor content (g-H<sub>2</sub>O/m<sup>3</sup>-gas) mixed with a dry aerosol at 298 K and cooled to  $T_f = 243$  K with  $T_c = 271$  K. The water bands at 3500 cm<sup>-1</sup> and 1650 cm<sup>-1</sup> increase in intensity while the gas-phase H<sub>2</sub>O features remain constant, which is consistent with the increasing conversion from a crystalline to an aqueous phase at constant water activity (i.e., the deliquescence process). The asymmetric 1420 cm<sup>-1</sup> ammonium peak also indicates the presence of (NH<sub>4</sub>)<sub>2</sub>SO<sub>4</sub>(s). Besides these direct spectroscopic characterizations, we note that the freezing behavior is entirely different from the aqueous aerosol described for Figure 4 (see section 3.3).

For mixed aerosol #1, the mass balance for water suggests that the ammonium sulfate should be completely deliquesced even at the lowest water vapor loading of 2.8 g-H<sub>2</sub>O/m<sup>3</sup>-gas, which greatly exceeds the aerosol loading of 0.3 g-particles/m<sup>3</sup>-gas. However, the spectral evidence noted in the preceding paragraph provides direct evidence of the presence of crystalline (NH<sub>4</sub>)<sub>2</sub>SO<sub>4</sub>(s). The conclusion is that there must be other water vapor sinks. A likely sink is the accumulation from previous experiments of an ammonium sulfate detritus, which forms a ubiquitous surface lining in the apparatus. At 298 K, vapor exchange with walls is rapid (e.g., the principle of the operation of a diffusion dryer).

An important additional point is that  $x^*$ , when determined by the water-to-sulfate ratio method (section 2.4.1), varies from top-to-bottom in Figure 5. In fact, the actual mole fraction of the aqueous phase is constant, as follows from Gibbs phase rule (omitting Kelvin effects) for this binary system when two condensed-phases are present. This problem in  $x^*$  arises because the IR spectra include contributions from both the crystalline and the aqueous ammonium sulfate components of the aerosol, whereas the calibration curve is only for the aqueous portion.

**3.2.2. Mixed Aerosol #2.** The IR spectra shown in Figure 6

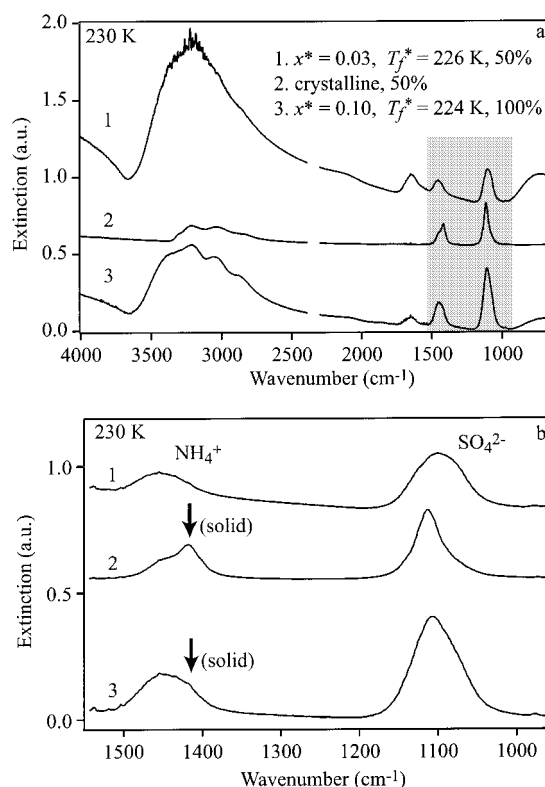


**Figure 6.** IR spectra of mixed aerosol #2 at  $T_f = 230$  K. (a) 1, IR spectrum of an aqueous aerosol ( $x^* = 0.03$ ,  $T_f^* = 226$  K). 2, IR spectrum of dry aerosol. 3, IR spectrum of an externally mixed aerosol when humid and dry flows are combined ( $x^* = 0.10$ ,  $T_f^* = 224$  K). (b) Expanded spectral region for ammonium (1420 cm<sup>-1</sup>) and sulfate (1100 cm<sup>-1</sup>) regions (gray bar). Arrows indicate spectral features characteristic of crystalline ammonium sulfate. Conditions:  $T_c = 271$  K, 3 slpm, 0.3 g-particles/m<sup>3</sup> gas,  $6 \times 10^6$  #-particles/cm<sup>3</sup>-gas. Spectra are offset for clarity.

6a-1) ( $x^* = 0.03$ ,  $T_f^* = 226$  K), a second containing crystalline particles (Figure 6a-2), and a third prepared by mixing secondary flows #1 and #2 at 230 K (Figure 6a-3) ( $x^* = 0.10 \pm 0.015$ ,  $T_f^* = 224$  K). Secondary flow #1 (dry) and #2 (humid) are generated from the aerosols shown in Figures 6a-1,2, with the exception of a decrease in flow rate from 3 to 1.5 slpm for each secondary flow. The asymmetric 1420 cm<sup>-1</sup> ammonium peak (arrows shown in Figures 6b-2,3) shows the presence of crystalline (NH<sub>4</sub>)<sub>2</sub>SO<sub>4</sub>. Further evidence for the presence of (NH<sub>4</sub>)<sub>2</sub>SO<sub>4</sub>(s) is shown in Figure 7-3, where the ferroelectric phase is apparent at 210 K.

### 3.3. Freezing Characteristics of the Three Aerosol Types.

The freezing characteristics (both  $T_f^*$  values and IR spectra) of the three aerosol types differ markedly due to their distinct physicochemical features. Figure 7 shows the IR spectra at 210 K after ice freezing is complete (cf. Figure 4b) for the three aerosol types, all of which have  $x^* = 0.11 \pm 0.01$  according to the composition calibration (which is carried out at warmer temperatures during the same experiment but prior to any ice freezing; see section 2.6). The  $T_f^*$  values are 216, 220, and 224 K for the aqueous aerosol, mixed aerosol #1, and mixed aerosol #2, respectively. The aerosol containing only aqueous particles shows the deepest apparent supercooling. The  $T_f^*$  values at other  $x^*$  values are summarized in Figure 8.

Figure 7b shows an expanded spectral region for the ammonium and the sulfate peaks of all these aerosol classes at 210 K. The solid arrows clearly indicate the formation of a crystalline ferroelectric phase in mixed aerosols #1 and #2. In



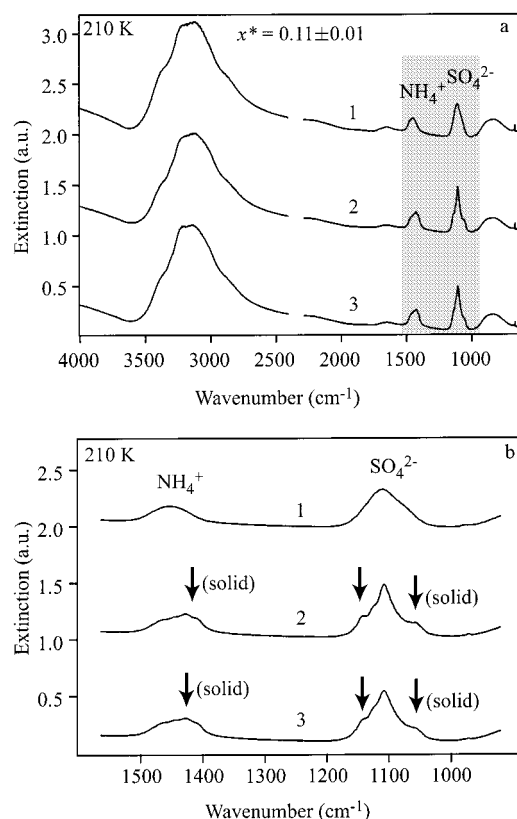


**Figure 7.** Further evidence on the mixing state of the aerosol is provided by the IR spectrum at temperatures below the ice freezing event. (a) IR spectra at  $T_f = 210$  K of three aerosols with similar apparent composition ( $x^* = 0.11 \pm 0.01$ ) but composed of distinctly different particles: 1, aqueous particles ( $T_f^* = 216$  K); 2, Mixed aerosol #1 ( $T_f^* = 220$  K); 3, Mixed aerosol #2 ( $T_f^* = 224$  K). (b) Expanded spectral region for ammonium ( $1420\text{ cm}^{-1}$ ) and sulfate ( $1100\text{ cm}^{-1}$ ) regions (gray bar). Arrows indicate shoulders characteristic of crystalline ammonium sulfate at 210 K. Spectra are offset for clarity.

contrast, no crystalline ammonium sulfate is apparent at 210 K in the aerosol initially containing only aqueous particles.

## 4. Discussion

**4.1. Estimation of Nucleation Rates by Inversion of Freezing Data.** In theory, the variance plots in Figure 4b track the complete (i.e., 100%) conversion in the aerosol of aqueous water to ice. Figure 4b shows that the variance full bandwidth of the ice freezing event is about 5 K, which is larger than the apparatus temperature gradients of 1 K (cf. section 2.5). The 5 K bandwidth then provides information about the details of the ice freezing event itself. With the help of a model treatment, we invert the freezing bandwidth data to estimate volume nucleation rates as a function of temperature and composition,  $J(T, x)$ . The model, which is described fully in Hung and Martin,<sup>15</sup> sequentially includes (1) hydration of the crystalline particles, (2) homogeneous ice nucleation to form ice within some of the particles (as determined by Poisson statistics, the candidate  $J(T, x)$  value, particle diameter, and residence time), and (3) vapor-phase mass transfer of  $\text{H}_2\text{O}$  from aqueous to ice particles.

The y-coordinate for the ice freezing event is the ice mass fraction of condensed-phase  $\text{H}_2\text{O}$  in the aerosol,  $F_I$ . The area under the variance curve is thus understood as unity ice mass fraction freezing. By this understanding, each temperature step downward provides an incremental increase in  $F_I$ . Figure 4b is thus the first derivative of  $F_I$  with temperature. We employ this

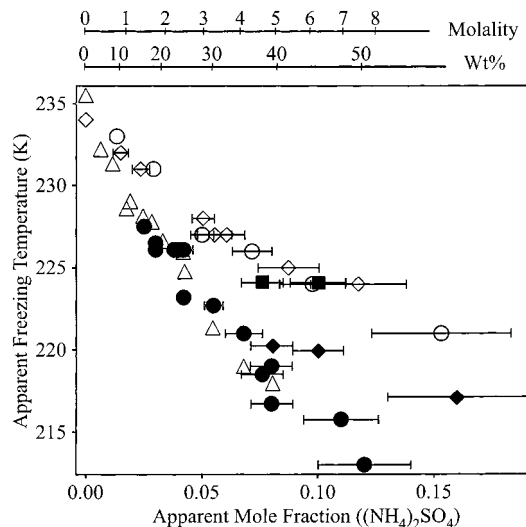


**Figure 8.** Summary of  $T_f^*$  results reported for several aerosol flow tube experiments. Present work: aqueous particles (●), mixed aerosol #1 (◆), and mixed aerosol #2 (■). Also shown are Chelf and Martin<sup>14</sup> (○), Cziczo and Abbatt<sup>13</sup> (◇), and Prenni et al.<sup>12</sup> (△). Note that each cited work defines  $T_f^*$  somewhat differently. See sections 4.2 and 4.3.

interpretation to invert the freezing data to estimate  $J(T)$ . The process is shown in Figure 9a, in which an analytic function (viz. a Gaussian fit to the data) approximates the data at a single mole fraction composition. The integrated  $F_I$  is shown in Figure 9b. At 1 K temperature intervals,  $F_I$  is simulated in an iterative fashion for different test  $J$  values until agreement is obtained with Figure 9b. Repetition of this process at several temperatures yields the  $J(T)$  function. Similar calculations are carried out at several other mole fraction compositions. The results are summarized in Figure 9c. (The  $J$ -values for  $x^* = 0$  are calculated according to Tabazadeh et al.<sup>9</sup>)

The simulation of the ice freezing event employs several simplifications, which partially contribute to the uncertainty indicated by the gray bars in Figure 9c. The simplifications are as follows. Each simulation is initiated with the same dry aerosol, whose number size distribution is measured with the SMPS. The distribution is characterized by a 300 nm diameter mode size having a geometric standard deviation of 1.7 and a total particle concentration of  $6 \times 10^6$  particles/ $\text{cm}^3$ -gas. To obtain the desired apparent mole fraction composition (e.g.,  $x^* = 0.07$ ) for a simulation run, the dry aerosol is hydrated. The simulation temperature is then dropped from  $T_c$  to  $T_f$ . For simplicity in these simulations, both the Kelvin effect and water vapor condensation are omitted during the temperature drop. At  $T_f$ , the homogeneous nucleation event occurs. The magnitude of this event is regulated by the choice of the  $J$  value, which is the parameter iteratively optimized, and by the time period allowed for nucleation (40 s). Another critical uncertainty is the decoupling of the nucleation and mass transfer events.<sup>15</sup>

According to our previous modeling work,<sup>15</sup> there is only a weak sensitivity of the results on the time period (varied from 30 to 120 s) for the homogeneous nucleation and vapor-phase mass transfer events. The transit time of the particles from the cold region of the freezing cell to the center of the observation cell is 40 s, though the extinction spectrum averages across the length (including the center region) of the observation cell. In comparison to the residence time, the freezing event is much more sensitive to  $T$  because  $J(T)$ , which regulates the homogeneous nucleation event, and  $P_{\text{H}_2\text{O}}(T)$ , which regulates the vapor-phase mass transfer, depend hyperexponentially and exponentially, respectively, on  $T$ .

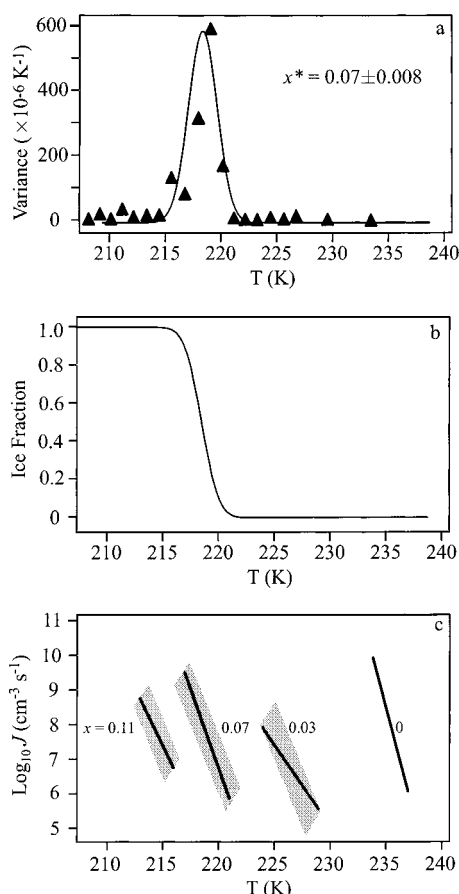


**Figure 9.** Inversion of the ice mass fraction freezing data to estimate rates of homogeneous nucleation. (a) Gaussian fit to the differential ice mass fraction freezing data (viz. variance plot from Figure 4b) ( $x^* = 0.07$ ). (b) Integration of the Gaussian fit. (c)  $J$  values ( $\text{cm}^{-3} \text{ s}^{-1}$ ) optimized in the simulation to agree with Figure 9b (i.e., data inversion) ( $x^* = 0.07$ ). Calculations are also reported for  $x^* = 0.03$  and 0.11. The  $x^* = 0$  data (i.e., pure water) are from the model of Tabazadeh et al.<sup>9</sup> Gray parallelograms depict the uncertainty in the  $J$ -values obtained from the inversion calculation.

The single largest uncertainty in the model treatment is likely the effective mass accommodation coefficients ( $\alpha$ ) employed in the vapor-phase mass transfer event. The  $\alpha$  values applied in the inversion analysis are unity for all of the aqueous concentrations and temperatures. Some support for  $\alpha = 1$  for water vapor condensation on ice is found for the case that ice growth in the aerosol flow tube is described as a “cold mixed phase cloud.” In this case, according to Nelson and Baker,<sup>23</sup> vapor diffusion is the dominant impedance in ice growth, and  $\alpha = 1$  for water vapor on ice is accurate. This scenario is appropriate at the high far-field supersaturations and cold temperatures inside the AFT.

**4.2. Apparent Freezing Temperatures in Several Experimental Apparatus.** As reported earlier,<sup>15</sup> we wish to know if a single  $J$ -function can reconcile the different  $T_f^*$  values reported in several experimental apparatus, including AFT-IR, CFD, OM, and DSC. Freezing events in each of these techniques occur at different  $J$ -values for several reasons, including different characteristic particle sizes (e.g., 300 nm versus 10  $\mu\text{m}$ ) and different sensitivities to ice freezing events (e.g., 50% by mass in DSC versus 1 particle in 1000 in CFD-0.001). Ice freezing events for  $(\text{NH}_4)_2\text{SO}_4/\text{H}_2\text{O}$  particles are indicated in the several apparatus for threshold  $J$ -values ( $\text{cm}^{-3} \text{ s}^{-1}$ ), as follows:  $10^6$  to  $10^8$  (revised for current work),  $10^9$  to  $10^{12}$ ,  $10^8$ , and  $10^8$ ,

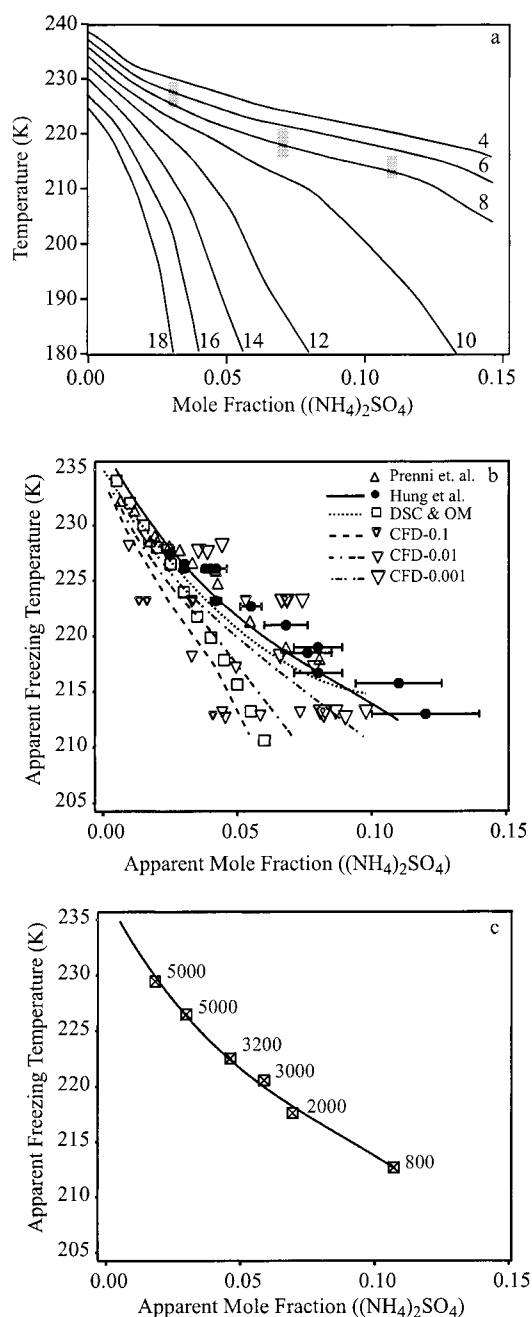


**Figure 10.** Simulation results for ice freezing events of  $(\text{NH}_4)_2\text{SO}_4/\text{H}_2\text{O}$  particles in several experimental apparatus. (a) The  $J$ -nucleation function ( $J(T,x)$ ) optimized to minimize the difference between observed and simulated apparent freezing temperatures. Contours of constant  $\log J$  ( $\text{cm}^{-3} \text{ s}^{-1}$ ) are shown. Gray bars show constraints imposed from the inversion results (Figure 9c). (b) Comparison between  $T_f^*$  values experimentally reported and those simulated based upon the optimized  $J$ -function. Points: ice formation in  $(\text{NH}_4)_2\text{SO}_4/\text{H}_2\text{O}$  particles observed by OM and DSC ( $\square$ ),<sup>10</sup> CFD ( $\nabla$ ,  $\triangledown$ ,  $\triangledown$ ),<sup>11</sup> and AFT-IR (Prenni et al.,<sup>12</sup> Cziczo and Abbatt,<sup>13</sup> Chelf and Martin,<sup>14</sup> and the current work) ( $\Delta$ ,  $\diamond$ ,  $\circ$ ,  $\bullet$ ). The lines indicate the model simulation results based on the  $J$ -function shown in part (a). (c) The figure notation  $N$  is interpreted as follows. When one of  $N$  particles nucleates ice homogeneously in the AFT-IR experiment, then there is sufficient residence time (40 s) in the observation cell for vapor diffusion from the remaining aqueous particles such that an ice freezing event will be observed (i.e., 50% ice mass fraction freezing).

respectively, for AFT-IR, CFD, OM, and DSC.<sup>15</sup> (The  $J$ -value range of  $10^6$  to  $10^8$  for AFT-IR is the revised recommendation based on the change from 10% to 50% for ice mass fraction freezing as the definition of  $T_f^*$  [cf. section 3.1].)



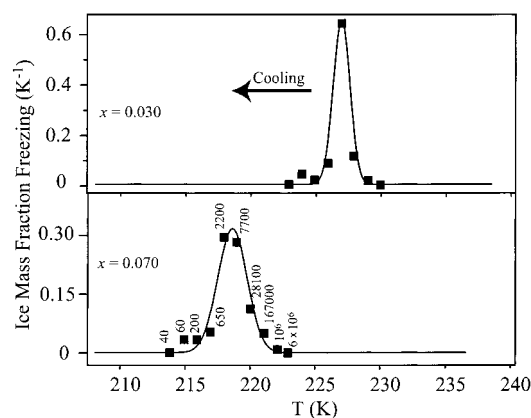


**Figure 11.** Simulation results of ice mass fraction freezing as  $T_f$  decreases in the aerosol flow tube experiment for  $x^* = 0.030$  (top) and  $0.070 \pm 0.003$  (bottom). The  $J$ -nucleation function shown in Figure 10 is employed. The particle size distribution is initialized from SMPS measurements. The ice freezing event is simulated at each temperature for 40 s. The  $N$  values are denoted for the results for  $x^* = 0.070$  (see Figure 10 caption). Solid lines serve to guide the eyes and do not represent a model fit.

Figure 10a shows the trial  $J$ -function that is constrained by the  $J$  values in Figure 9c and optimized to agree with the  $T_f^*$  values of CFD, OM, and DSC. The optimized  $J$  function minimizes the sum of the squares of the differences between the simulated and the reported  $T_f^*$  values for the several experimental apparatus. The AFT-IR data of refs 13 and 14 are omitted in the current analysis because we wish to focus on the aerosol class containing only aqueous particles (see section 4.3). A residence time of 40 s is employed for the homogeneous ice nucleation and the vapor-phase mass transfer events, as consistent with the new apparatus (20 s shorter than our earlier work<sup>15</sup>).

The comparison between the simulated and the reported  $T_f^*$  values is shown in Figure 10b, based upon the optimized  $J$  function in Figure 10a. The  $T_f^*$  values of the simulations and the experiments agree well for CFD-0.1 and CFD-0.01. However, for CFD at the 0.1% detection level (viz. CFD-0.001), the simulated  $T_f^*$  values are cooler than the experimental results. In contrast, the simulated  $T_f^*$  values are warmer than the observations for both OM and DSC. These results are consistent with the conclusions of Hung and Martin:<sup>15</sup> the  $T_f^*$  values reported for ice freezing events in  $(\text{NH}_4)_2\text{SO}_4/\text{H}_2\text{O}$  particles for several experimental apparatus do not appear to be self-consistent.

The number  $N$  is provided next to selected points in Figure 10c. When one of  $N$  particles nucleates ice, then there is a sufficient residence time (40 s) in the observation flow cell for vapor diffusion from the remaining aqueous particles such that an ice freezing event is observed (i.e., 50% ice mass fraction). Figure 10c shows there is a monotonic decrease in  $N$  with decreasing temperatures, which results from the diminishing contribution of mass transfer to the freezing event as water vapor pressure falls with temperature, as discussed by Hung and Martin.<sup>15</sup> The  $N$  values in the current study are about one decade lower than the earlier work,<sup>15</sup> which arises both from the shorter residence time (40 s compared to 60 s) and the criterion for  $T_f^*$  (50% compared to 10% ice formation).

The  $J$  function from Figure 10a is employed to simulate the ice freezing fractions for  $x^* = 0.03$  and  $0.07$  as a function of temperature (Figure 11) (cf. Figure 4b). A residence time of 40 s and  $\alpha = 1$  are employed. The plot shows the temperature-normalized  $F_1$  as a function of  $T_f$ . There is good qualitative

agreement between the bandwidths of the simulation (Figure 11) and those of the measurements (Figure 4b) for  $x^* = 0.07$ . However, the simulated bandwidth is narrower than observations for  $x^* = 0.03$ .

Figure 11 shows that one particle in  $10^6$  freezes by homogeneous nucleation on the warm side of the Gaussian peak for  $x^* = 0.070$ ; the remainder of the ice freezing event originates from vapor-phase mass transfer from the remaining aqueous particles to the ice particles. In contrast, on the cold side of the Gaussian peak, homogeneous nucleation provides an important direct contribution to the freezing event, in which one particle in 10 freezes by homogeneous nucleation. These same general features are also true at more dilute concentrations (e.g.,  $x^* = 0.030$  in Figure 11), though there is an overall relative shift favoring larger contributions from vapor-phase mass transport in the freezing event due to the increase in water vapor pressure. The associated effect is a sharpening in the freezing bandwidth from about 5 K for  $x^* = 0.070$  to 2 K for  $x^* = 0.030$ . Prenni et al.<sup>12</sup> report a decrease from 6 to 2 K in the freezing bandwidth as  $x^*$  decreases.

There is one final issue to emphasize with regard to sections 4.1 and 4.2. For the aqueous aerosol, common sense and the model treatment both suggest that at sufficiently low temperatures (e.g., 210 K), homogeneous ice nucleation in each aqueous particle should be rapid and 100% of the particles should form ice (i.e., 1 particle in 1 in relation to the preceding discussion of 1 in  $N$ ). In this case, we would also expect ammonium sulfate to crystallize, and the ferroelectric form should then be present at low temperature. In fact, as reported in section 3.3, the aqueous phase is still present at 210 K following the ice freezing event for the aqueous aerosol. From this result, two conclusions can be reached. First, the model treatment is not complete because its predictions differ from some of the observations. Important factors that the model does not treat include physical mixing of air parcels, vapor-phase mass transfer to the walls, coupled freezing and vapor-phase mass transport, and smooth cooling (i.e., the homogeneous nucleation event in the model simulation occurs only at the lowest temperatures). In reality, a possible explanation consistent with the observations is that, due to the aforementioned omitted factors, one particle in many nucleates ice prior to others and begins to grow by vapor-phase mass transport of  $\text{H}_2\text{O}$  from evaporating aqueous particles. The remaining aqueous particles increase in their mole fraction composition and thus are less likely to nucleate ice. These particles are physically separate from ice and indefinitely metastable: there is no foreign surface for the heterogeneous crystallization of ammonium sulfate. According to this explanation, the aqueous phase is then still present at 210 K, as consistent with observations. Related to this insight is the second conclusion: this explanation provides indirect support of the validity of the vapor-phase transport model such that the freezing of one particle in many yields an ice freezing event in the IR spectra.

The possibility of homogeneous nucleation of crystalline ammonium sulfate in the aqueous particles at 210 K should also be considered. If the aqueous phase is in equilibrium with ice at 210 K, its aqueous mole fraction composition is 0.2,<sup>24</sup> absent Kelvin effects. The saturation ratio with respect to the paraelectric phase is 23.2, yet crystal formation does not occur during the residence time in the AFT. Onasch et al.<sup>25</sup> and Cziczó and Abbatt<sup>13</sup> show that crystallization is not rapid until the saturation ratio approaches 35, at least at 233 K. Thermodynamic information on the ferroelectric phase is unavailable, but the saturation ratio is certainly larger than 23.2, as pursuant with

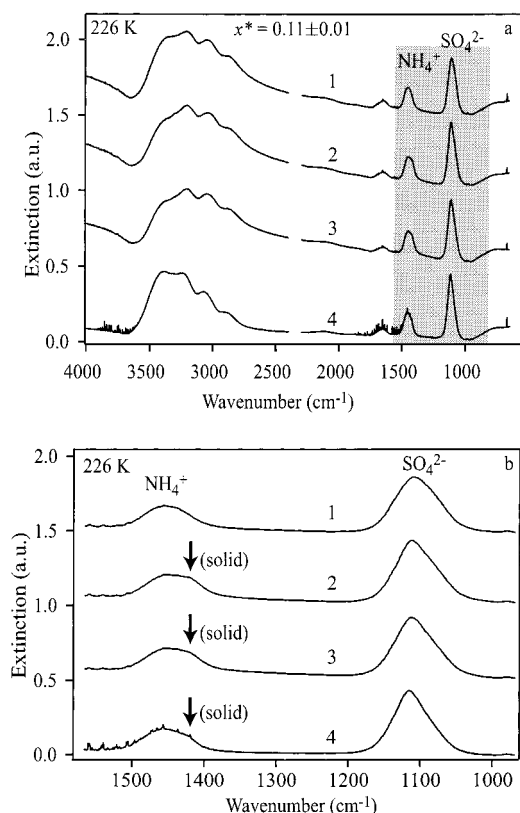


**Figure 12.** Comparison at  $T_f = 226$  K, which is prior to the ice freezing event, of the IR spectra of the aerosol of the current study with the IR spectrum of the aerosol employed by Chelf and Martin.<sup>14</sup> (a) IR spectra of four aerosols with similar apparent composition ( $x^* = 0.11 \pm 0.01$ ) but composed of distinctly different particles: 1, aqueous particles ( $T_f^* = 216$  K); 2, mixed aerosol #1 ( $T_f^* = 220$  K); 3, mixed aerosol #2 ( $T_f^* = 224$  K); 4, Chelf and Martin's preparation<sup>14</sup> ( $T_f^* = 223$  K). (b) Expanded spectral region for ammonium (1420 cm<sup>-1</sup>) and sulfate (1100 cm<sup>-1</sup>) regions (gray bar). Arrows indicate shoulders characteristic of crystalline ammonium sulfate.

the basic principles of thermodynamics for reasonable physical parameters, because the paraelectric phase is metastable with respect to the ferroelectric phase at 210 K.

**4.3. Comparisons with other Aerosol Flow Tube Experiments.** A compilation of the results obtained in the current study, as well as by other workers employing AFT-IR, is shown in Figure 8 for the ice freezing experiments with (NH<sub>4</sub>)<sub>2</sub>SO<sub>4</sub>/H<sub>2</sub>O particles. Our current results for an aerosol containing solely aqueous particles appear to agree with the work of Prenni et al.<sup>12</sup> Our current results for mixed aerosol #2 apparently agree with the Chelf and Martin<sup>14</sup> results, as well as similar earlier results reported by Cziczko and Abbatt.<sup>13</sup>

**4.3.1. Chelf and Martin.** An explanation is now apparent to explain the warm freezing results of Chelf and Martin.<sup>14</sup> Figure 12 shows spectra having in common  $x^* = 0.11 \pm 0.01$  at  $T_f = 226$  K for the three aerosol classes employed in the current study and for a similar aerosol from the Chelf and Martin<sup>14</sup> study. The presence of crystalline (NH<sub>4</sub>)<sub>2</sub>SO<sub>4</sub> in the Chelf and Martin study is apparent in the 1420 cm<sup>-1</sup> peak shape of the ammonium ion (arrow in Figure 12b-4). Furthermore,  $T_f^* = 223$  K for Chelf and Martin's report,<sup>14</sup> which agrees well with  $T_f^* = 224$  K for the mixed aerosol #2 (q.v. section 3.3). We conclude that Chelf and Martin<sup>14</sup> studied an aerosol containing both crystalline and aqueous particles. The effect of a mixed state aerosol is that the reported  $x^*$  values for the aqueous portion of the aerosol are systematically too large, due to the contribution of crystalline

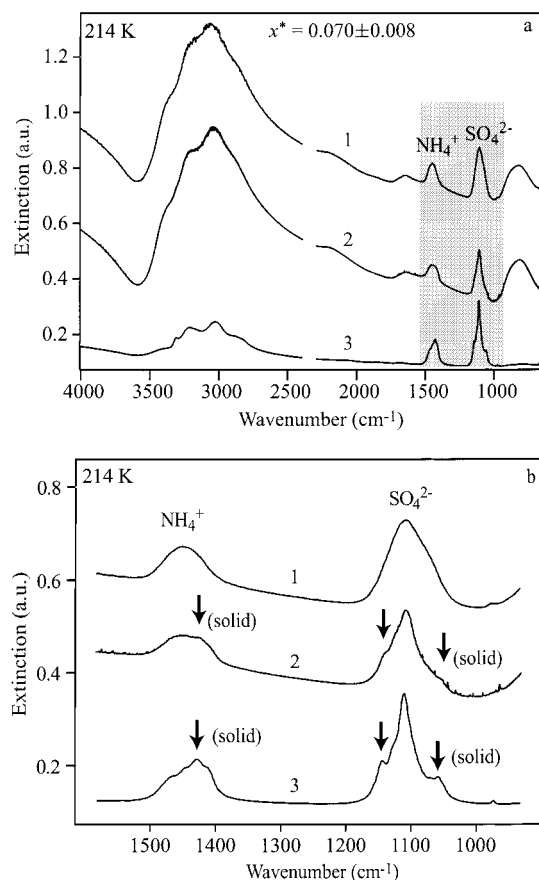


**Figure 13.** Comparison at  $T_f = 214$  K, which is cooler than the ice freezing event, of the IR spectra of the aerosol of the current study with the IR spectrum of the aerosol employed by Chelf and Martin.<sup>14</sup> (a) IR spectra of two aerosols with similar apparent compositions ( $x^* = 0.07 \pm 0.008$ ) and a crystalline particle reference: 1, aqueous particles ( $T_f^* = 221$  K); 2, Chelf and Martin's preparation<sup>14</sup> ( $T_f^* = 227$  K); 3, crystalline particles. (b) Expanded data for ammonium (1420 cm<sup>-1</sup>) and sulfate (1100 cm<sup>-1</sup>) regions (gray bar). Arrows indicate shoulders characteristic of crystalline ammonium sulfate.

particles to the recorded IR spectra. Qualitative correction for this error shifts the  $T_f^*$  curve of Chelf and Martin in Figure 8 to more dilute concentrations, which is in better agreement with the current study on aqueous aerosols. Quantitative correction requires a measure of  $x^*$  of the aqueous component of the aerosol; an estimate could be made if the fractional crystalline content of the aerosol were known. (The light scattering contribution to Figure 12a-4 is much less than in the other spectra because of changes in the particle number size distribution. A TSI 3076 atomizer is employed in the current study to generate aerosol, whereas Chelf and Martin employed a vapor condensation method.)

An additional insight is provided by examining the spectra of Chelf and Martin after the ice freezing event, as shown in Figure 13. The aerosols in the current study and in Chelf and Martin are both characterized at temperatures prior to freezing and have similar apparent compositions ( $x^* = 0.070 \pm 0.008$ ). After ice freezing (e.g., 214 K), however, the aqueous aerosol of the current study retains aqueous ammonium sulfate particles (cf. Figure 13a-1 and discussion of Figure 7 in section 3.3). In contrast, the spectrum of the Chelf and Martin aerosol shows crystalline phase features, as revealed by the ferroelectric transitions (cf. Figure 13b-2). The conclusion is again that Chelf and Martin studied an aerosol containing both crystalline and aqueous particles.

4.3.2. *Czizco and Abbatt.* The  $T_f^*$  values of Czizco and Abbatt,<sup>13</sup> which are similar to those of Chelf and Martin,<sup>14</sup> suggest that an aerosol containing both crystalline and aqueous particles was studied. Section 3.4, "Static Mode," of ref 13 appears to corroborate this conclusion. In that work the ferroelectric features appear in an aerosol cooled to 219 K. If the aerosol were initially aqueous, crystallization by efflorescence would not be expected because the water activity falls to only 0.6.<sup>13,25</sup> Hence, the formation of the ferroelectric phase suggests that a paraelectric crystalline phase was initially present. These results are analogous to the discussion of Figure 13 of the current paper. Our detailed investigations (e.g., Figure 3) also reaffirm that the para- to ferroelectric transition is not kinetically inhibited and occurs at 223 K; Czizco and Abbatt report the transition at 219 K, which probably indicates temperature uncertainties in their apparatus. An additional point is that the efflorescence experiments (e.g., Figure 13 of ref 13) are also consistent with an aerosol initially containing a fraction of externally mixed crystalline particles (e.g., see Martin et al.<sup>26</sup> for  $F < 1$ , where  $F$  is the fraction of total particles containing a solid inclusion). That is, the accuracy of the efflorescence work in ref 13 precludes neither a mixed state aerosol nor the interpretation offered by us for the static mode experiments.

For a mixed state aerosol,  $x^*$  depends on the fraction of crystalline material in the aerosol. The apparent close agreement between the  $\{x^*, T_f^*\}$  values of Czizco and Abbatt<sup>13</sup> and those of Chelf and Martin<sup>14</sup> at first suggests similar quantities of crystalline material in the aerosols. However, the evidence in this regard is mitigated by two facts. First, the shallow slope (i.e.,  $dT_f^*/dx^*$ ) apparent in Figure 8 for these two sets of results indicates a low sensitivity on the crystalline fraction. Second, the error bars on the  $x^*$  values also render less certain any apparent agreement. For these reasons the crystalline fractions in the aerosols studied by Czizco and Abbatt<sup>13</sup> and those of Chelf and Martin<sup>14</sup> may still be somewhat different while still yielding results that appear similar in a representation such as Figure 8.

4.3.3. *Prenni et al.* Figure 8 shows that the  $\{x^*, T_f^*\}$  values for the aqueous aerosol of the current work appear to agree with those of Prenni et al.<sup>12</sup> Prenni kindly provided us with high-resolution spectra from his data in Figure 3 of ref 12, and the features of crystalline ammonium sulfate are absent. The Prenni et al. spectra agree with those shown by us in Figure 12 for an aerosol composed of aqueous particles.

This exceptionally good apparent agreement between our results for aqueous particles and those of Prenni et al. is unexpected: Prenni et al. report  $T_f^*$  values as the onset of freezing (i.e., the foot in Figure 4b) whereas the  $T_f^*$  values in the current work are reported for 50% ice mass fraction freezing. According to Figure 4b, there is a 2–3 K difference between these two endpoints. Such a difference does not occur in the  $T_f^*$  values shown in Figure 8. This result can be explained by considering  $x^*$  for the two investigations. Analysis of the provided spectrum by Prenni (viz. Figure 3 of ref 12) by the approach described in section 2.4.1 yields  $x^* = 0.036$ , whereas Prenni et al. report  $x^* = 0.018$  (12 wt %). When we extend this analysis to the results shown in Figure 8, the data points for Prenni et al. shift to higher  $x^*$  values, which then places the reported  $T_f^*$  values of that work 2 to 3 K warmer than the values of the current work. Based on Figure 4b, just that difference would be expected based upon the differences in the definition of  $T_f^*$  (viz. the onset of freezing versus 50% ice mass fraction freezing).

The related question is why we find  $x^* = 0.036$ , whereas Prenni et al. report  $x^* = 0.018$ . Prenni et al. estimate composition by assuming equilibrium with ice on the walls in the conditioning tube, whereas we estimate the composition from the spectroscopic features. We speculate that either  $x^*$  changes from 0.018 in the conditioning cell to 0.036 in the observation cell of Prenni et al. or the particles of Prenni et al. are small enough that a water vapor pressure corresponding to  $x^* = 0.018$  over a flat surface equilibrates with  $x^* = 0.036$  over a curved surface due to the Kelvin effect. The second possibility seems very likely, requiring a 2% water vapor pressure correction. Such a correction corresponds to roughly 100 nm diameter aqueous particles for typical surface tensions, though measurements by Prenni et al. suggest particles closer to 300 nm.

In a model treatment, Hung and Martin<sup>15</sup> consider how  $x^*$  values might differ when estimated from the IR bands (AFT-IR-1) (i.e., the current study) as compared to the assumption of equilibration with ice on the walls at higher temperatures (AFT-IR-2) (i.e., a method similar to Prenni et al.). All other factors being equal, Hung and Martin conclude that  $x^*(\text{AFT-IR-1}) < x^*(\text{AFT-IR-2})$ . As described above, our analysis of the spectra of Prenni et al. provides the opposite conclusion that  $x^*(\text{AFT-IR-1}) > x^*(\text{AFT-IR-2})$ . To address this discrepancy, of first importance is that the analysis in the two preceding paragraphs is based upon the experimental observations and is thus the standard against which to compare the simulation results. Because those results do not agree with the observations, the simulation appears to be missing a physical component. The most notable omission is the absence of cryogenic pumping of water vapor from the aerosol to the ice on the walls (i.e., the vapor pressure of the aqueous aerosol is greater than the vapor pressure of ice on the walls). As such, when the aerosol cools, water vapor condenses on the aerosol (instead of the walls) and  $x^*$  dilutes. The model simulation then concludes  $x^*(\text{AFT-IR-1}) < x^*(\text{AFT-IR-2})$ , due to the respective determinations of  $x^*(\text{AFT-IR-1})$  and  $x^*(\text{AFT-IR-2})$  at cold and warm temperatures. At the other extreme, if all excess vapor is scavenged by the walls, then we obtain  $x^*(\text{AFT-IR-1}) > x^*(\text{AFT-IR-2})$  due to the Kelvin effect, which is implicitly included in -IR-1 and explicitly excluded in -IR-2. That the observations obey this second inequality suggests that an improved future simulation would include spatially dependent components, rather than the current box model implementation, to incorporate vapor exchange with the walls. It is worth emphasizing that at the first level of inquiry the  $\{x^*, T_f^*\}$  values of this work agree well with Prenni et al., as well as with the simulation of Hung and Martin, and that the detailed considerations in the last few paragraphs take the comparisons to a higher standard in a deeper level of inquiry.

4.3.4. *Comparison with H<sub>2</sub>SO<sub>4</sub>/H<sub>2</sub>O Aerosols.* As compared to (NH<sub>4</sub>)<sub>2</sub>SO<sub>4</sub>/H<sub>2</sub>O aerosols, the freezing results based on AFT-IR measurements for H<sub>2</sub>SO<sub>4</sub>/H<sub>2</sub>O aerosols agree much better.<sup>12,27–29</sup> This consistency may arise because no solid phase is believed to form in H<sub>2</sub>SO<sub>4</sub>/H<sub>2</sub>O aerosols (i.e., SAT and SAH nucleation is usually kinetically inhibited) prior to the freezing event. The consistency may also arise for a second reason, as follows: if H<sub>2</sub>SO<sub>4</sub>/H<sub>2</sub>O particles homogeneously nucleate ice at lower temperatures than (NH<sub>4</sub>)<sub>2</sub>SO<sub>4</sub>/H<sub>2</sub>O (for same  $x^*$ ), then vapor-phase mass transfer will make a smaller quantitative contribution to the ice freezing event of H<sub>2</sub>SO<sub>4</sub>/H<sub>2</sub>O aerosols. The implication is that AFT-IR differences in apparatus geometry, aerosol loading, and other factors that affect mass transfer, but not homogeneous nucleation, will play a smaller role in the freezing events of H<sub>2</sub>SO<sub>4</sub>/H<sub>2</sub>O aerosols. In this case,



AFT-IR studies on  $\text{H}_2\text{SO}_4/\text{H}_2\text{O}$  aerosols would be more self-consistent than for  $(\text{NH}_4)_2\text{SO}_4/\text{H}_2\text{O}$  aerosols.

**4.3.5. Differences among Apparatus.** It is not obvious why the experiments of Czizco and Abbatt<sup>13</sup> and Chelf and Martin<sup>14</sup> yield aerosols containing both crystalline and aqueous particles while both the current work and that of Prenni et al.<sup>12</sup> yield aerosols containing aqueous particles only. However, the spectroscopic and freezing results appear to clearly indicate the differences. One key change in the new apparatus (see section 2.3), and also a feature of Prenni et al.,<sup>12</sup> is that the AFT is of constant diameter throughout all cold regions, thus supporting laminar flow while avoiding problems of ice plugging. The apparatus of Czizco and Abbatt<sup>13</sup> and of Chelf and Martin<sup>14</sup> both employ narrow junctions between the conditioning and the observation cells. These junctions plug and promote turbulent flow, which may influence the physical state of a fraction of the particles in the aerosol.

**4.4. Detailed Mixing State of Aerosols. 4.4.1. Description.** There are two likely scenarios for the detailed physical mixing characteristics of mixed aerosols #1 and #2: (a) some crystalline particles deliquesce completely, yielding an externally mixed aqueous/crystalline aerosol or (b) the outer regions of the crystalline particles deliquesce while retaining inner crystalline cores to yield an internally mixed aerosol. In our present work, we do not discriminate between these two possibilities. Under either scenario, the  $x^*$  of the mixed aerosols depends on the relative fraction of crystalline and aqueous particles and upon the mole fraction composition of the aqueous portion. The apparent freezing temperatures depend both on the internal or the external mixing state of the aerosol and on the aqueous mole fraction composition.

If the aerosol is externally mixed, the points shown in Figure 8 for Chelf and Martin<sup>14</sup> may translate freely along the  $x^*$ -axis at fixed  $T_f^*$ , as dependent on the crystalline fraction of the aerosol. In this case, the results for Chelf and Martin can be rationalized to be consistent with the results of the present work for aqueous particles. Alternatively, in the second case, if the aerosol is internally mixed, heterogeneous nucleation is likely important because the crystalline  $(\text{NH}_4)_2\text{SO}_4$  inside the aerosol particle may enhance ice formation at the interface. The complexity of heterogeneous nucleation is partially revealed in the recent paper of Zuberi et al.<sup>30</sup> We do not further address possible aspects of heterogeneous nucleation in this paper because the range of current experiments is insufficient for informed considerations.

**4.4.2. Modeling.** When we suppose an externally mixed aerosol, we conclude that the  $x^*$  values determined from the IR spectra require that the aqueous particles must have dilute mole fraction compositions so that the IR spectra of this portion of the aerosol, when combined with the contribution by crystalline ammonium sulfate particles ( $x = 1$ ), yields the observed  $x^*$ . A key point is that the aqueous composition must be more dilute than a saturated solution. Our conclusion is apparent from observing that the  $x^*$  values for many points are less than 0.08 for mixed aerosols #1 and #2 in Figure 8. Along the aqueous-crystalline coexistence line,  $dx/dT$  is sharp,<sup>5</sup> suggesting the coexistence mole fraction composition is approximately 0.08 at the observation temperatures below 233 K because the composition is 0.082 at the eutectic (253 K). The mixed aerosols are thus metastable because the water activity of a vapor-phase in equilibrium with the aqueous particles is sufficient thermodynamically to initiate deliquescence at the surface of the crystalline particles.<sup>29,31</sup> We emphasize that the IR spectra for these aerosols indicate that the crystalline phase

is indeed present. One possibility is that the metastable aerosol does not have sufficient residence time in the apparatus to complete vapor-phase mass transport from the aqueous particles to the crystalline particles. To address this possibility, we completed model calculations.

In the model, we treat the surface initiation step for deliquescence as instantaneous, at least by our available observational techniques, because we believe there is no nucleation barrier to the formation of a critical aqueous germ (i.e., the deliquescence nucleation event is fast).<sup>5,8,29,31</sup> After the formation of a germ, however, water vapor flux is required to support the continued expansion of the aqueous phase. It could be possible that the residence time within the IR cells is insufficient for vapor-phase mass transfer to occur to an appreciable extent from the aqueous to the deliquescing crystalline particles. If so, the crystalline particles, due to the time required for vapor-phase mass transport, would convert to a shell-core morphology of an aqueous outer layer and a crystalline inner core.

Figure 14 shows the results of the calculations for the mixing of two equal flows, the first containing aqueous particles and the second crystalline particles. In the simulation, we omit the details of the mixing process and assume complete mixing at zero time, i.e., the model is initiated with two bin sets, one of aqueous and the other of crystalline particles. Equal flows of aqueous ( $x^* = 0.03$ ) and crystalline particles are mixed at 225 K for 5 s. Nucleation of deliquescence is assumed to be instantaneous so long as the vapor-phase water activity is sufficient thermodynamically. The time period (5 s) for vapor-phase mass transfer from the aqueous to the deliquescing crystalline particles is shorter than the combined residence time in the freezing and the observation cells (40 s) because water vapor pressure falls once the ice freezing event is initiated by homogeneous nucleation. The result is to squelch deliquescence. In our simulation treatment, a decoupled model is implemented in which a possible deliquescence event is treated separately from the ice freezing event. The decoupled treatment provides some qualitative insights without the expectation of quantitative applicability. A decision is necessary about how long to run the simulation, at first for possible deliquescence, before switching the simulation over to possible homogeneous ice nucleation (which definitely occurs at 225 K and  $x^* = 0.03$ ). In the current work the sensitivity of the results to the selection of 5 s is not investigated. The number- and mass-size distributions for aqueous particles in the humid aerosol, prior to mixing with the crystalline particles of the dry aerosol, are shown in Figure 14a. The IR extinction is weighted by mass. The mass size distribution shown in Figure 14a thus indicates that the supermicron particles contribute most significantly to the recorded IR spectrum.

Employing the simulation described by Hung and Martin<sup>15</sup> for several values of  $\alpha$ , Figure 14b shows the averaged aqueous mole fraction composition in many size bins for the two components of the aerosol, including particles initially crystalline and initially dilute aqueous. At long times when the aerosol approaches equilibrium (dotted line;  $x = 0.058$  with Kelvin effect omitted), the two components of the aerosol are indistinguishable, provided a sufficient water reservoir exists in the aqueous fraction to fully deliquesce the crystalline fraction (as is true in the present simulation). The average mole fraction compositions ( $y$ -axis coordinate) for the bins of the initially crystalline aerosol are calculated from averaging the contributions of the crystalline and the aqueous components, while the average mole fraction composition for the aqueous bins is simply

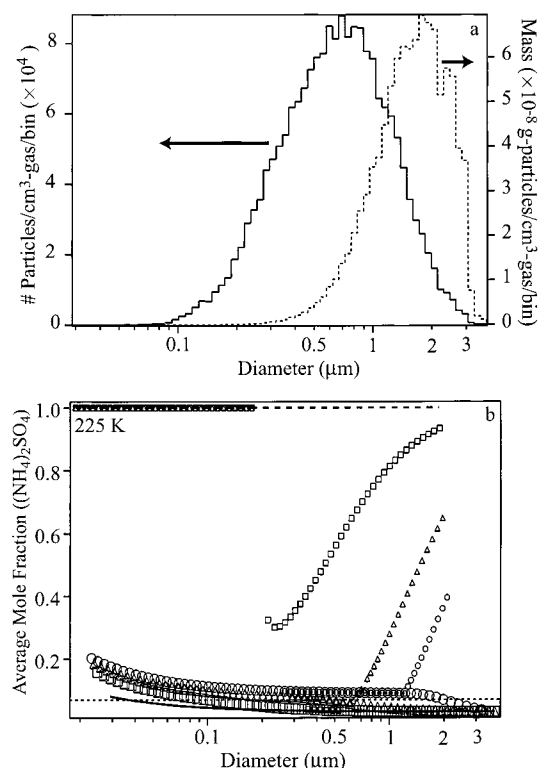


**Figure 14.** Simulation of vapor-phase mass transfer effects on particle composition when equal flows of aqueous and crystalline particles mix at  $T_f = 225$  K (i.e., simulation of mixing secondary flows #1 and #2). (a) The number and mass size distributions for an aerosol containing aqueous particles prior to mixing ( $x^* = 0.03$ ). Because the IR detection method responds proportionally to mass, the mass size distribution shows that those particles greater than  $1 \mu\text{m}$  contribute mostly strongly to an observed IR extinction spectrum of the aerosol. (b) The dependence on particle diameter of the bin-averaged aqueous mole fraction composition (see text), both before and after mixing. The distributions prior to mixing are indicated by lines for aqueous (line) and crystalline (dashed line) particles. After mixing the symbols (large symbols for initially aqueous particles and small symbols for initially crystalline particles) show the simulated aqueous concentrations (5 s residence time in freezing cell prior freezing) ( $\circ$ ,  $\alpha = 1$ ;  $\triangle$ ,  $\alpha = 0.1$ ;  $\square$ ,  $\alpha = 0.01$  for mass accommodation coefficient  $\alpha$ ). If  $\alpha \leq 0.1$ , these calculations conclude that slow vapor-phase mass transfer inhibits deliquescence during the residence time in the aerosol flow tube at 225 K. The dotted line shows the compositions at long times ( $x = 0.058$ ) (i.e., an equilibrated aerosol when the Kelvin effect is omitted). For the parameters chosen, the aerosol is composed entirely of aqueous particles at equilibrium, which is not attained in the simulation.

the aqueous mole fraction composition. The average mole fraction is calculated from the number of moles of  $(\text{NH}_4)_2\text{SO}_4$  in both the aqueous and the crystalline states divided by this quantity plus the moles of  $\text{H}_2\text{O}$  in the aqueous phase.

The results show that the two components of the aerosols remain highly distinct (i.e., characterized by different mole fractions) for  $\alpha \leq 0.1$ , where the average mole fraction for the initially crystalline particles remains significantly above the equilibrium composition, especially in the mass mode, which is the mode of importance both for the IR spectrum and the homogeneous nucleation event that begins the ice freezing event. The simulations thus indicate the aerosol is externally mixed so long as  $\alpha \leq 0.1$ . Particles smaller than 100 nm do not deliquesce in the model treatment because the Kelvin effect is applied only to the aqueous particles, which has the effect of increasing the deliquescence relative humidity.

The true value of  $\alpha$  is uncertain. It is believed that  $\alpha$  of water vapor condensation on water droplets is approximately 0.06.<sup>32–34</sup>

Several arguments support the likelihood that  $\alpha$  for water condensation on aqueous ammonium sulfate droplets is lower than 0.06. First, to the extent that a salt may be regarded as an impurity, impurities usually reduce  $\alpha$ .<sup>32</sup> Second, Prenni et al.<sup>12</sup> note that the residence time in the conditioning region for aqueous ammonium sulfate aerosol must be increased significantly, as compared to sulfuric acid aerosol, to obtain equilibrium with ice. If sulfuric acid, as an upper limit, is considered equivalent to water, then the implication is that  $\alpha$  for aqueous ammonium sulfate is smaller. Third, Shulman et al.<sup>35</sup> have directly observed unexpectedly small  $\alpha$  for the evaporation of aqueous ammonium sulfate droplets. Evaporation and condensation coefficients are often taken as equal.<sup>32</sup> When taken together, these factors arguably suggest the mass accommodation coefficient of water condensation on aqueous ammonium sulfate surfaces is less than 0.10 and likely less than 0.01.

There are several additional interesting features in Figure 14b. According to the assumptions of our model, small diameter crystalline particles do not deliquesce due to the Kelvin effect.<sup>36</sup> This simulation result disagrees with recent experimental observations, which find deliquescence of smaller particles more favorable.<sup>37</sup> This disagreement probably arises because our calculations include a Kelvin correction for the aqueous particles but omit a similar size-dependent effect on the free energies of the crystalline particles.<sup>38,39</sup> Figure 14b also shows that for high mass transfer rates (e.g.,  $\alpha = 1$ ) water vapor rapidly hydrates the initially crystalline particles. The aqueous concentrations of the largest particles (both crystalline and aqueous) undergo the smallest changes due to the large mass reservoirs, as compared to the finite water flux. The competing Kelvin effect for small particles and mass transfer effects for large particles yield composition accommodation most rapidly for intermediately sized crystalline particles.

The simulation results are sensitive to the composition- and temperature-dependent aqueous surface tensions. However, the aqueous surface tensions of ammonium sulfate, especially at low temperatures and for supersaturated results, are not well known.<sup>37</sup> We employ the function given in our earlier work.<sup>15</sup> If the true aqueous surface tensions are greater than those employed in the simulation, deliquescence is thermodynamically less favorable (i.e., an extension of the Kelvin-effect-inhibited no-deliquescence line in Figure 14b to larger diameters) with the associated effect that  $\alpha$  could exceed 0.1 while slow vapor-phase mass transfer would still inhibit deliquescence due to the increased surface tensions.

## 5. Conclusions

The following conclusions are drawn from the current work. (1) The differences in the apparent freezing temperatures of  $(\text{NH}_4)_2\text{SO}_4/\text{H}_2\text{O}$  aerosols, as reported for several aerosol flow tube experiments,<sup>12–14</sup> arise principally from the physical makeup of the aerosol. For an aqueous aerosol,  $x^*$  is accurately obtained from an IR calibration curve of band ratios. For a mixed-phase aerosol containing both crystalline and aqueous particles,  $x^*$  values obtained by the same calibration method are in error. (2) When the ice freezing event is understood within the paradigm of a homogeneous nucleation event followed by a vapor-phase mass transfer event, the AFT-IR technique is useful for measuring  $J$  values for homogeneous ice nucleation of  $10^6$  to  $10^{10} \text{ cm}^{-3} \text{ s}^{-1}$ . (3) Ice mass fraction freezing data inferred from analysis of the IR spectra can be inverted by a model simulation to estimate  $J$  values as a function of temperature. (4) Due to vapor-phase mass transfer, the AFT-IR technique can be sensitive to the freezing of one in  $10^6$  particles,

especially at low freezing ice mass fractions (i.e., the warm side of the differential ice mass fraction freezing distribution, as in Figure 11). (5) Although this paper appears to reconcile qualitatively the AFT-IR results for  $(\text{NH}_4)_2\text{SO}_4/\text{H}_2\text{O}$  aerosols, Figure 10b shows further work is necessary to reconcile AFT-IR, OM, DSC, and CFD measurements. (6) The experimental results are consistent with an intrinsic water mass accommodation coefficient of under 0.1 on the surface of aqueous ammonium sulfate and an effective water mass accommodation of unity on the surface of ice under the conditions typical of an AFT-IR experiment.

For aerosols containing particles that do not form crystalline phases under conditions present in the AFT experiment (e.g.,  $\text{H}_2\text{SO}_4/\text{H}_2\text{O}$ ), cognizance of the physical makeup of the aerosol (point 1 above) is not relevant. However, when studying freezing of most salts (e.g.,  $(\text{NH}_4)_2\text{SO}_4/\text{H}_2\text{O}$ ,  $\text{NaCl}/\text{H}_2\text{O}$ , and so on), the experimenter must remain vigilant of the physical makeup of the aerosol: the apparent mole fraction assignments based on the ratio of IR bands do not discriminate among aerosol classes and thus lead to erroneous composition assignments when the aerosol is not physically homogeneous.

**Acknowledgment.** We thank Paul DeMott and an anonymous reviewer for valuable comments and suggested improvements for the manuscript. We are grateful for support received from the NSF Atmospheric Chemistry Program, a Presidential Early Career Award in Science and Engineering (PECASE), and the New York Community Trust Merck Fund.

## Appendix. List of Symbols and Abbreviations

- AFT-IR: Aerosol flow tube infrared spectroscopy.  
 AFT-IR-1: AFT-IR with aqueous particle composition determined from the condensed-phase IR spectrum.  
 AFT-IR-2: AFT-IR with aqueous particle composition determined from the assumption of equilibrium with ice at  $T_c$ .  
 CFD: Continuous flow thermal diffusion chamber.  
 CFD-0.001: CFD method with the threshold level of 0.1% of particles frozen.  
 CFD-0.01: CFD method with the threshold level of 1% of particles frozen.  
 CFD-0.1: CFD method with the threshold level of 10% of particles frozen.  
 DSC: Differential scanning calorimetry.  
 $F$ : The fraction of total particles containing a solid inclusion.  
 $F_I$ : The ice mass fraction of condensed-phase  $\text{H}_2\text{O}$  in the aerosol.  
 IR: Infrared.  
 $J$ : Volume nucleation rate for ice nucleation from an aqueous medium ( $\text{cm}^{-3} \text{s}^{-1}$ ).  
 LT: Low temperature.  
 MCT-A: Mercury cadmium telluride, type A detector.  
 $N$ : When one of  $N$  particles nucleates ice, then there is a sufficient residence time (40 s) in the observation flow cell for vapor diffusion from the remaining aqueous particles such that an ice freezing event will be observed (i.e., 50% ice mass fraction).  
 OM: Optical microscopy.  
 RH: Relative humidity.  
 SMPS: Scanning mobility particle sizer.  
 $T$ : Temperature (K).  
 $T_c$ : Conditioning temperature (K).  
 $T_f$ : Candidate freezing temperature (K).  
 $T_f^*$ : Apparent freezing temperature (K).  
 $T_{\text{H}_2\text{O}}$ : Total water vapor loading ( $\text{g-H}_2\text{O}/\text{m}^3 \text{ gas}$ ).

- $x$ : Mole fraction of solute.  
 $x^*$ : Apparent mole fraction of solute.  
 $\alpha$ : Mass accommodation coefficient.

## References and Notes

- (1) Seinfeld, J. *National Research Council, Panel on Aerosol Radiative Forcing and Climate Change. A Plan for a research program on aerosol radiative forcing and climate change*; National Academy Press: Washington, DC, 1996.
- (2) Houze, R. A. J. *Cloud Dynamics*; Academic Press: San Diego, 1993; Vol. 53.
- (3) *Aerosol-Cloud-Climate Interactions*; Hobbs, P. V., Ed.; Academic Press: San Diego, 1993.
- (4) Goody, R. *Principles of Atmospheric Physics and Chemistry*; Oxford University Press: New York, 1995.
- (5) Martin, S. T. *Chem. Rev.* **2000**, *100*, 3403–3453.
- (6) Rogers, D. C.; DeMott, P. J.; Kreidenweis, S. M.; Chen, Y. *Geophys. Res. Lett.* **1998**, *25*, 1383–1386.
- (7) DeMott, P. J.; Rogers, D. C.; Kreidenweis, S. M.; Chen, Y.; Twohy, C.; Baumgardner, D.; Heymsfield, A. J.; Chan, K. R. *Geophys. Res. Lett.* **1998**, *25*, 1387–1390.
- (8) Martin, S. T. *Geophys. Res. Lett.* **1998**, *25*, 1657–1660.
- (9) Tabazadeh, A.; Martin, S. T.; Lin, J. S. *Geophys. Res. Lett.* **2000**, *27*, 1111–1114.
- (10) Bertram, A. K.; Koop, T.; Molina, L. T.; Molina, M. J. *J. Phys. Chem. A* **2000**, *104*, 584–588.
- (11) Chen, Y. L.; DeMott, P. J.; Kreidenweis, S. M.; Rogers, D. C.; Sherman, D. E. *J. Atmos. Sci.* **2000**, *57*, 3752–3766.
- (12) Prenni, A. J.; Wise, M. E.; Brooks, S. D.; Tolbert, M. A. *J. Geophys. Res.* **2001**, *106*, 3037–3044.
- (13) Cziczo, D. J.; Abbatt, J. P. D. *J. Geophys. Res.* **1999**, *104*, 13781–13790.
- (14) Chelf, J. H.; Martin, S. T. *J. Geophys. Res.* **2001**, *106*, 1215–1226.
- (15) Hung, H.-M.; Martin, S. T. *J. Geophys. Res.* **2001**, *106*, 20379–20394.
- (16) Krause, E. *Computational fluid dynamics and reacting gas flows. In Computational Fluid Dynamics and Reacting Gas Flows*; Engquist, B., Luskin, M., Majda, A., Eds.; Springer-Verlag: New York, 1988.
- (17) Jain, Y. S.; Bist, H. D.; Upreti, G. C. *Chem. Phys. Lett.* **1973**, *22*, 572–575.
- (18) Jain, Y. S.; Bist, H. D. *Phys. Status Solidi B* **1974**, *62*, 295–300.
- (19) Hoshino, S.; Vedam, K.; Okaya, Y.; Pepinsky, R. *Phys. Rev.* **1958**, *112*, 405–412.
- (20) O'Reilly, D. E.; Tsang, T. J. *J. Chem. Phys.* **1967**, *46*, 1291–1300.
- (21) O'Reilly, D. E.; Tsang, T. J. *J. Chem. Phys.* **1967**, *46*, 1301–1304.
- (22) Clapp, M. L.; Miller, R. E.; Worsnop, D. R. *J. Phys. Chem.* **1995**, *99*, 6317–6326.
- (23) Nelson, J. T.; Baker, M. B. *J. Geophys. Res.* **1996**, *101*, 7033–7047.
- (24) Clegg, S. L.; Brimblecombe, P.; Wexler, A. S. *J. Phys. Chem. A* **1998**, *102*, 2137–2154. See <http://www.hpc1.uea.ac.uk/~e770/aim.html>.
- (25) Onasch, T. B.; Siefert, R. L.; Brooks, S. D.; Prenni, A. J.; Murray, B.; Wilson, M. A.; Tolbert, M. A. *J. Geophys. Res.* **1999**, *104*, 21317–21326.
- (26) Martin, S. T.; Han, J. H.; Hung, H. M. *Geophys. Res. Lett.* **2001**, *28*, 2601–2604.
- (27) Cziczo, D. J.; Abbatt, J. P. D. *Geophys. Res. Lett.* **2001**, *28*, 963–966.
- (28) Bertram, A. K.; Patterson, D. D.; Sloan, J. J. *J. Phys. Chem.* **1996**, *100*, 2376–2383.
- (29) Braban, C. F.; Cziczo, D. J.; Abbatt, J. P. D. *Geophys. Res. Lett.* **2001**, accepted.
- (30) Zuberi, B.; Bertram, A. K.; Koop, T.; Molina, L. T.; Molina, M. J. *J. Phys. Chem. A* **2001**, *105*, 6458–6464.
- (31) Fortin, T. J.; Shilling, J. E.; Tolbert, M. A. *J. Geophys. Res.*, submitted.
- (32) Marek, R.; Straub, J. *Int. J. Heat Mass Transf.* **2001**, *44*, 39–53.
- (33) Shaw, R. A.; Lamb, D.; Moyle, A. M. *J. Atmos. Ocean. Technol.* **2000**, *17*, 940–948.
- (34) Shaw, R. A.; Lamb, D. J. *J. Chem. Phys.* **1999**, *111*, 10659–10663.
- (35) Shulman, M. L.; Charlson, R. J.; Davis, E. J. *J. Aerosol. Sci.* **1997**, *28*, 737–752.
- (36) Chen, J. P. *J. Atmos. Sci.* **1994**, *51*, 3505–3516.
- (37) Hameri, K.; Vakeva, M.; Hansson, H. C.; Laaksonen, A. *J. Geophys. Res. Atmos.* **2000**, *105*, 22231–22242.
- (38) Lasaga, A. C. *Kinetic Theory in the Earth Science*; Princeton University Press: Princeton, N. J., 1998.
- (39) Mirabel, P.; Reiss, H.; Bowles, R. K. *J. Chem. Phys.* **2000**, *113*, 8200–8205.